Dual stimulus responsive borosilicate glass (BSG) scaffolds promote diabetic alveolar bone defectsrepair by modulating macrophage phenotype

Pengfei Tian [a],[1], Limin Zhao [b],[1], Jua Kim [a], Xian Li [a], Chunyu Liu [a], Xu Cui [a], Tao Liang [a], Yunbo Du [b], Xiehui Chen [b], Haobo Pan [a],[c],[*]

[a] Center for Human Tissues and Organs Degeneration, Shenzhen Institute of Advanced Technology, Chinese Academy of Sciences, Shenzhen, 518055, PR China
[b] Shenzhen Longhua District Central Hospital, Shenzhen, 518000, PR China
[c] Shenzhen Healthemes Biotechnology Co. Ltd, Shenzhen, 518102, PR China

ARTICLE INFO

ABSTRACT

The regeneration of alveolar bone is still clinical challenge, particularly accompanied with diabetes, causing metabolic disorder with a protracted low-grade inflammatory phenotype. As a result, the anticipated loading of biomaterials is highly suspicious in spontaneous modulation of cells function, which is mostly disturbed by constant inflammation. In this study, we developed glucose and hydrogen peroxide dual-responsive borosilicate glass (BSG) scaffolds loaded with epigallocatechin gallate (EGCG) to synergistically modulate the abnormal inflammation of diabetic alveolar bone defects. It was found that the release of EGCG by BSG could directly regulate the shift of macrophages from M1 to the M2 phenotype by promoting autophagy and lessening the inhibition of autophagic flux. Moreover, EGCG can also indirectly regulate the polarization phenotype of macrophages by reducing the activation of NF-κb in stem cells and restoring its immunoregulatory capacity. Therefore, the addition of EGCG to BSG scaffold in diabetes allows for a more striking modulation of the macrophage phenotype in a timely manner. The altered macrophage phenotype reduces local inflammation and thus increases the ability to repair diabetic alveolar bone, showing promise for the treatment of alveolar defect in diabetic patients.

1. Introduction

Diabetes is a heterogeneous disease characterized by high blood glucose levels and caused by absolute and relative deficiencies of insulin [1]. The number of people with diabetes has increased globally in recent decades, from 108 million in 1980 to 463 million in 2019. By 2045, the figure will rise to over 700 million [2]. Diabetes frequently causes abnormal bone metabolism or peri-implant inflammation due to hyperglycemia, resulting in serious alveolar bone loss in the implant area, and ultimately resulting in bone integration and implant failure [3,4]. Moreover, large defects of alveolar bone often fail to mend naturally through the body's restorative mechanisms [5]. Therefore, the restoration of large alveolar bone defect in a persistent inflammatory environment is a major clinical challenge that directly affects the stability of further treatment.

Bone graft therapy is one of the most effective methods to treat bone defects in oral and maxillofacial region. Among the many treatments available, autologous bone is widely used to treat bone defects due to no risk of disease transmission and immune rejection. However, the main issue of autologous bone graft is the inadequate source and donor site-related complications. Allograft bone, although relatively adequate, is believed to raise the risk of immune rejection and infection [6]. With the rapid advancement of biomaterials, artificial bone scaffolds have demonstrated significant promise as an alternative to cure alveolar bone defects, including collagen fibers, gelatin, glass ceramics, and artificial polymers. Among them, borosilicate glass (BSG) containing a double network of $[BO_3]$ and $[SiO_4]$ exhibits an incredibly adjustable degradation rate to match bone growth rate by accurately adjusting the composition of the glass network [7,8]. As such, BSG's promotion of osteogenesis is predictable, but whether it is sufficient to regulate

complex inflammation in the diabetic milieu remains a question. In fact, osteogenesis may be hampered in DM, in which the function of cells is regrettably impeded or at least disordered [9].

Inflammation induced by oxidative stress is an influential risk factor for the exacerbation of diabetic complications [10,11]. Pro-inflammatory growth factors such as TNF-α, IL-6 and IL-1b are assumed to be the primarily factors responsible for the activation of the pro-inflammatory transcription factor nuclear factor-kappa B (NF-κb) [12]. Nuclear factor-κb (NF-κb) is a transcription factor that reacts to various stimuli and regulate transcription associated with inflammation [13]. Numerous studies have shown that aberrant activation of NF-κb is a potential mechanism for the failure to resolve inflammation in diabetic trauma and the disruption of the repair and regeneration balance in vivo [14,15]. The regression of inflammation is an essential component of tissue regeneration, which is mediated by the timely clearance of debris by hyperinflammatory macrophages and the transition to an anti-inflammatory phenotype [16]. The tissue is excessively destroyed and healing is delayed by dysfunctional macrophages, which is directly linked to abnormal transcription of NF-κb. In diabetes, the immunomodulatory role of mesenchymal stem cells on macrophages is similarly impacted by aberrant NF-κb transcription, which in turn further disrupts the resolution of local inflammation [15].

In this study, we, therefore, developed a BSG-PBA-PVA system with ROS and glucose response and loaded EGCG into it. The aforementioned system was dispersed into photosensitive silk protein and then formed into a scaffold by DLP molding and inserted into the alveolar bone defect of diabetic rats. By releasing EGCG, the BSG-PBA-PVA system more actively reduced mitochondrial reactive oxygen species and inhibited NF-κb activation. The reduction in macrophage mitochondrial ROS may be achieved by increasing autophagy and restoring autophagic flow, which in turn directly improves the macrophage inflammatory phenotype. Additionally, the restoration of immunomodulatory function of BMSCs by EGCG may be indirect reason of the inflammatory phenotype of macrophages. Finally, we used a streptozotocin-induced alveolar bone defect model in diabetic rats to investigate the therapeutic efficiency and possible mechanisms of EGCG-loaded ROS and glucose dual-responsive borosilicate glass in modulating macrophage phenotype and promoting alveolar bone regeneration.

2. Materials and methods

2.1. Materials

All chemicals with analytical reagent grade were used without further extracts, including tetraethyl orthosilicate (TEOS) (Aladdin, China), triethyl phosphate (TEP) (Aladdin, China), tributyl borate (TBB) (Aladdin, China), carboxyphenylboronic acid (Aladdin, China), 3-aminopropyltriethoxysilane (APTES) (Aladdin, China), Polyvinyl alcohol (Aladdin, China), Silk protein, Lithium bromide (Meryer, China), Glycidyl methacrylate (GMA, USA), Lithium phenyl (2,4,6-trimethylbenzoyl) phosphate (LAP) (Sigma-Aldrich, USA). Calcium nitrate tetrahydrate (Aladdin, China), epigallocatechin gallate (EGCG, Aladdin, China). Cell Viability Kit-8 (cck; Beyoncé; China). Mito-tracker-green (M7514), Mito-tracker-red (M7512), Mito SOX™ Red (M36008) and Lysotrackers (L7526) were purchased from Thermo Fisher. JC-1 probe (C2005) and AdPlus-mCherry-GFP-LC3B (C3012) was from Beyotime. Different antibodies like NF-κB p65 (8242S), Phospho–NF–κB p65 (3033S), IκBα (4814S), Phospho-IκBα (2859S), DRP1 (8570S), MFN2 (9482S), LC3 (12741S), SQSTM1/p62 (23214S), iNOS (13120S), CD206 (24595S) were purchased from Cell Signaling Technology. F4/80 (30325S), CD86(PA5-88284), ARG(PA5-29645), PINK1 (PA1-16604), PARKIN (PA5-13399) were purchased from Thermo Fisher. CD90 (ab181469), sca1 (ab51317) were purchased from Abcam. ELISA kits for mouse TGF-β were obtained from Beyotime. Percent-positive cells and mean fluorescence intensity (MFI) were quantified using Fiji software.

2.2. Preparation and characterization of ABBSG (BSG-PBA-PVA)

According to previous work, borosilicate glass was prepared using the classical CTAB template, alkali-catalyzed sol-gel method. In the following way, 1.1 g of CTAB and 5 ml of ammonia were dissolved in 300 ml of aqueous ethanol (50%) at 40 °C. After the CTAB was completely dissolved, 4.3 ml of ethyl orthosilicate (TEOS), 0.7 ml of tributyl borate (TBB), and 0.4 ml (TEP) were dropped into the solution with rapid stirring. After 30 min of reaction, 1 g of calcium nitrate solution (2 ml) was added dropwise and stirred for 4 h. The powder was then centrifuged, washed 3 times with ethanol and deionized water, freeze-dried for 48 h, and finally sintered at 600 °C for 180 min (addition rate 2 °C/min) to obtain borosilicate glass (BSG).

The BSG was then chemically modified by grafting amino groups onto the BSG surface using APTES. 100 mg of BSG powder was dispersed in 10 ml of anhydrous ethanol. An anhydrous ethanol solution(2 ml) containing 8.5 μl of APTES was slowly dropped and stirred at room temperature for 12 h. Then the glass was centrifuged, washed three times with anhydrous ethanol and water, and dried at 60° to obtain the amino-grafted borosilicate glass. 100 mg of the NH₂-BSG was dispersed in 10 ml of dimethyl sulfoxide (DMSO) solution. In addition, 59 mg of carboxyphenylboronic acid, 276.2 mg of EDC hcl and 83.3 mg of NHS were weighed and dissolved in 10 ml of DMSO, stirred for 30 min, and then slowly dropped into a dispersion system of NH₂-BSG and stirred for 4 h at room temperature. The reaction solution was centrifuged, the precipitate collected and washed three times with water, and then freeze-dried for 24h to obtain a borosilicate glass modified with phenylboronic acid (BBSG). Finally, 100 mg of phenylboronic acid borosilicate glass was dispersed into a 4% aqueous PVA solution, stirred for 10min and then centrifuged and washed three times with water to obtain PVA-coated borosilicate glass (ABBSG). The intermediates and final products were analyzed using infrared spectroscopy (FTIR) (FT-IR Frontier, USA) external spectroscopy, UV–Vis spectrophotometry (Thermo 250 Xi, USA), and nuclear magnetism (NMR) (BRUKE AVANCE 400 MH, Switzerland) to further investigate the stepwise modification process. The major elements (Si, B, Ca, C) in the material were identified by X-ray photoelectron spectroscopy (XPS) (Thermo Scientific K-Alpha, USA). Bare BSG and BSG-PVA were observed before and after PVA encapsulation using transmission electron microscopy (TEM) (FEI Tecnai G2 F20 S-Twin 200 kV, USA). The samples were quantified by Thermal Gravimetric Analyzer (TGA) (Mettler TGA/DSC3+, Switzerland). The pore size of the particles was measured by a specific surface area and porosity analyzer (BET) (ASAP2460/2020, USA).

2.3. EGCG loading and release

Firstly, 4% PVA solution was prepared, and PBA modified BSG powder was mixed with PVA solution at 1:1 and quickly stirred for 10min to form PVA shell (ABBSG). To load EGCG, 100 mg of ABBSG and 10 mg of EGCG were entirely dispersed by sonication in 100 μl of water for 30min. The mixture was put in a vacuum drying oven, and the vacuum was repeated 3 times for 10–20 min each time to produce ABBSG containing EGCG. The mixture was then centrifuged, washed with water, and dried overnight in a vacuum oven at 50 °C and designated as ABBSG@EGCG. The loading rate of EGCG in ABBSG is calculated by the following equation:

$$Load\ efficiency = \frac{weight\ of\ EGCG\ in\ ABBSG}{Initial\ weight\ of\ the\ drug} \times 100\%$$

The morphology before and after encapsulation of EGCG was observed using TEM. Quantitative TGA analysis of loaded EGCG was performed. Given that EGCG is susceptible to oxidation when exposed to air leading to changes in the UV peak, the Bradford method was therefore used to observe changes in BSA in response to changes in high sugar solutions(30 mM) and H₂O₂ solutions (1 mM).

2.4. Scaffold construction and characterization

The scaffold consisted of photosensitized silk protein, ABBSG, ABBSG@EGCG, and β-TCP. SF-MA was based on the protocol described in the literature [17,18]. Lyophilized SF-MA was dissolved in water at a concentration of 15% w/v, and then 1% w/v of BSG was dispersed in the aqueous solution of SF-MA. The photo-initiator LAP (0.2% w/v) was then added until completely dissolved in the hydrogel prepolymer. Specimens were designed by BP-8600 (Engineering for life, China) as STL files. STL files were sliced in the z-direction. Finally, each layer is sliced and projected by a projector to form the 3D form of the design. Printing is carried out by repeating the projected image in the hydrogel and then increasing the z-level. The printing parameters were: printing thickness, 75 μm; the number of substrate layers, 3 layers; light intensity, 100 w/cm^2; single layer exposure time, 30 s. After printing, the printed object was briefly rinsed with deionized water to remove the unreacted solution. Finally, the scaffold is still named ABBSG, ABBSG@EGCG, and β-TCP, respectively. The extract is prepared in the ratio of 1g of the scaffold in 10 ml of the medium.

The compressive strength of the ABBSG scaffold was tested in a universal tester (ZHIQU Test Machine Inc). Scaffolds with 10 mm (diameter) dimensions and 8 mm (height) were studied in the compressive tests. A compression force was loaded at a displacement rate of 1 mm min^{-1} until the specimen broke to calculate the stress at failure and strain at failure.

To test the stability of the ABBSG scaffold in an SBF environment, we evaluated the swelling behavior of samples by soaking them into SBF for three days at 37 °C. Briefly, the scaffold (10 mm*10 mm*2 mm) with a weight of W0 was immersed into centrifuge tubes with 10 ml PBS and incubated at 37 °C for 24h. Then the sample was taken out, a filter paper blotted up the water on the surface, and the samples were weighed as Wt. The swelling ratio of the sample was expressed as the solvent absorption percentage and calculated following the equation:

$$Swelling\ ratio = \frac{Wt - W0}{Wt} \times 100\%$$

To determine the ion solubilisation of borosilicate glasses in hydrogels, the ion release (represented by Si, B and Ca ions) from silk protein scaffolds containing ABBSG in phosphate-buffered saline (PBS) was characterized by inductively coupled plasma optical emission spectrometry (ICPOES, PerkinElmer Optima 7000DV). Briefly, 0.5 g of hydrogel scaffold (~Φ = 10 × 10 mm) was immersed in 6 ml of PBS. Every 1 day 1 ml of PBS was removed for ICP testing and 1 ml of fresh PBS was added to the immersion solution (n = 3). The pH changes in the different fractions were also recorded.

2.5. Cell culture

In this study, we chose RAW264.7 macrophages and mouse-derived mesenchymal stem cells(mBMSCs) to test the biological role of the material in diabetes. RAW264.7 was obtained from the Chinese Academy of Sciences and cultured in Dulbecco's Modified Eagle Medium (DMEM, Hyclone, USA) containing 10% (v/v) fetal bovine serum (FBS, Gibco) and 1% (v/v) penicillin-streptomycin (P/S). The mBMSCs were obtained from the Chinese Academy of Sciences and cultured in a-(a-MEM, Hyclone, USA) containing 10% (v/v) fetal bovine serum (FBS) and 1% (v/v) penicillin-streptomycin (P/S). In the experiment, raw264.7 and BMSCs were incubated continuously in low (5 mmol) and high (30 mmol) glucose conditions for 3d.

2.6. Phenotypic alterations in macrophages

In vitro experiments showed that macrophages were stimulated by high glucose to mimic the diabetic environment. The extracts (ABBSG, ABBSG@EGCG, and β-TCP) were then added to the medium, and the culture was continued for 3 d. Protein levels (iNOS, CD86, ARG and CD206) were analyzed by Western blotting, using F-action as an internal reference. mRNA levels (TNF-a, Il-1β, IL-6, iNOS, Arg, CD206, BMP-2) were analyzed by qPCR, RNA splitting, and cDNA preparation were manufactured according to the manufacturer. Quantitative RT-PCR was performed using Fast SYBR Green primer sequences listed in the Supplementary Table 1. Data were normalized by housekeeping genes.

2.7. Quantitative mitochondrial morphology

RAW264.7 cells and BMSCs were cultured in confocal dishes (NEST). After incubating for 30min at 37 °C , the mitochondria were visualized using Mito-Tracker Green, and images were acquired using confocal microscopy. Ten random cells from each sample were analyzed to identify cells that underwent mitochondrial fragmentation. The morphology of mitochondria was quantified using Fiji software.

2.8. Detection of cell proliferation and apoptosis

Cell viability was assessed by the CCK8 assay. mBMSCs Cells were inoculated in 96-well plates containing 2×10^3 cells per well. After 1,3,5 d of incubation, cck8 solution was added to the cells in proportion to the manufacturer's instructions and quantified at 450 nm using an ELISA microplate reader (model) Results were expressed as OD values.

mBMSCs (2×10^4/well) were seeded in 24-well plates and were incubated at 37 °C for 24h. Then the cells were incubated with 4.5 mM glucose (normal glucose, NG) or 30 mM glucose (high glucose, HG) for 3d and subsequently replaced with extracts (ABBSG, ABBSG@EGCG, and β-TCP). After incubation for 3d, BrdU incorporation was assayed according to the protocol of BeyoClick™ EdU Cell Proliferation Assay Kit. Fluorescence images were captured by fluorescence microscope (Olympus, Japan), and the fluorescence intensity (MFI) was quantified using Fiji software.

Annexin V-FITC/PI apoptosis Kit was used to analyze the apoptosis of mBMSCs under high glucose conditions. Briefly, 5×10^5 mBMSCs/well were implanted into 6-well plates. After incubation for 24h, cells were incubated with 4.5 mM glucose (normal glucose, NG) or 30 mM glucose (high glucose, HG) for 3d. Then the culture was changed to the extracts (ABBSG, ABBSG@EGCG, and β-TCP) and continued for 3 days. Annexin V-FITC and propidium iodide (PI) were added according to the manufacturer's instructions and incubated at 4 °C for 15 min after rinsed in phosphate buffered saline. The cells were analyzed by flow cytometry (Bection Dickinson, San Jose, CA).

2.9. Measurement of mitochondrial membrane potential

The mitochondrial membrane potential is measured by a dual fluorescent potential sensitive fluorescent probe, JC-1. At high mitochondrial membrane potentials, JC-1 aggregates in the mitochondrial matrix, forming a polymer that produces red fluorescence (590 nm); at low mitochondrial membrane potentials, JC-1 fails to aggregate in the mitochondrial matrix, when it produces green fluorescence (529 nm). Briefly, JC-1 (5 μl/ml) was added to the cell culture medium and incubated at 37° for 30min, then observed by confocal microscopy. Mitochondrial polarization was expressed as a ratio of red/green fluorescence intensity. The fluorescence intensity was detected by Fiji software.

2.10. ELSA detection

BMSCs cells were seeded in 6-well plates and continued to be cultured for 4 d after the cells reached convergence by adding low sugar (5 mmol) and high sugar (30 mmol) media, respectively. Subsequently, the medium was replaced with the extract medium of (ABBSG, ABBSG@EGCG, and β-TCP) and incubation continued for 3d. The medium from each group was collected and centrifuged. Finally, the expression of the soluble cytokine TGF-β in the culture medium was measured using

an ELISA kit according to the manufacturer's instructions.

2.11. GFP-RFP-LC3 analysis

The number of autophagic vesicles and autophagic lysosomes was assessed using mGFP-RFP-LC3 adenovirus. RAW264.7 was transduced for 24h according to the manufacturer's instructions and then exposed to HG medium for 96h before subsequent experiments. After treatment, cells were imaged under a confocal microscope at excitation/emission wavelengths of 514nm/529 nm for GFP and 585/590 nm for RFP. All samples were examined under confocal microscopy, and yellow overlap points were counted using Fiji software.

2.12. Immunofluorescence

RAW264.7 cells were treated and incubated using Mito Tracker red at 37 °Cfor 30min, fixed in 4% paraformaldehyde for 30min, then permeabilized using Immunostaining Permeabilization for 10min and closed using Quick Block™ Blocking Buffer for 10min. Cells were then immunolabelled using LC3 antibody (1:200) overnight at 4 days. After washing, incubate with FITC-coupled secondary antibody for 1h at 37 °C. Fluorescence signals were detected using laser confocal microscopy, and co-localization coefficients were scored using Fiji software.

2.13. Detection of lysosomes

RAW264.7 cells were treated with both Mito Tracker green and lysotracker red and incubated for 30 min at 37 °C. The fluorescence signal was examined using a laser confocal microscope, and co-localization coefficients were determined using Fiji software.

2.14. Western blot analysis

Cells were homogenized in RIPA lysate containing PMSF. Proteins were collected by centrifugation at 12,000 rpm at 4 °C and then boiled for 10 min. Mitochondrial proteins are extracted according to the protocol of Cell Mitochondria Isolation Kit (beytime, China). Briefly, equal amounts of proteins were separated on sodium dodecyl sulfate-polyacrylamide gel electrophoresis (SDS-PAGE), transferred to nitrocellulose membranes (PVDF), and then incubated with appropriate primary antibodies (p-p65, Phospho-IκBα, DRP1, MFN2, PINK1, PARKIN) and secondary antibodies were incubated. Blots were visualized with Immobilon western n C semi luminescent HRP substrate.

2.15. Animal experiments

To evaluate the effect and possible mechanism of EGCG on the repair of alveolar bone defects in diabetic rats. Sprague- Dawley (S D) male rats were selected for animal experiments and were purchased from Beijing Vitehe Laboratory Animal Technology Co. All experiments were performed at the Shenzhen Institute of Advanced Technology (SIAT) of the Chinese Academy of Sciences in accordance with the regulations of the SIAT Animal Research Committee.

The type 2 diabetic rat model in this experiment was established by intraperitoneal injection of a low dose of streptozotocin (65 mg/kg) (Sigma), according to a previous study. Animals were considered diabetic when the blood glucose was over 22 mM 1 week after injection and raised for 8 weeks prior to surgery. Eighteen male rats were selected for the experiment and randomly divided into 3 groups. Subsequently, the rats were anaesthetized with isoflurane gas, and a 3mm × 5 mm bone defect was created on the buccal side of the rat's mandible. After implantation of scaffolds containing ABBSG, ABBSG@EGCG, and β-TCP, respectively, the rats were executed at 1 week, 4 weeks, and 8 weeks, and the rat mandibles were obtained and fixed using 4% paraformaldehyde. The tissue samples were embedded in paraffin blocks and cut into sections of 4 μm thickness. These sections were processed and stained with HE, Safranin O-Fast Green, and Goldner stains. Immunofluorescence staining was performed using the following primary antibodies: *anti*-f4/80, anti-cd206, anti-cd86, *anti*-LC3, anti-CD90, *anti*-sca-1, *anti*-TNF-α, and *anti*-TGF-β.

2.16. Micro-computer tomography (Micro-CT) analysis

A μX-ray 3D image system (SCANCO Medical AG μCT 100, Switzerland) was used to acquire images of the alveolar bone at a voltage of 70kv. The isotropic resolution of scanning was 7.4 μm. The RAW data were imported into CT-Analyzer 1.18.4.0 (Voluem Graphics, UK) analysis, and the corresponding 3D reconstruction images were used to determine the bone mass of the alveolar bone. First, the ratio of solid to tissue volume (BV/TV), trabecular thickness (Tb. Th), trabecular number (Tb. N), and trabecular separation (Tb. Sp) were calculated.

2.17. Statistics analysis

Prism software (GraphPad version 8.0.2) was used for statistical analysis. All data were expressed as mean ± standard deviation. Levene's test was first used to determine the homogeneity of variance. When the results of the test were expressed as P values > 0.05, this indicated equal variance within the group. One-way analysis of variance (ANOVA) was then used to determine between-group differences. If P values < 0.05, this indicated that the within-group variance was not equal, and the Brown-Forsythe and Welch ANOVA test was used. *P*-value <0.05 indicated a statistical significance.

3. Result

3.1. Construction of EGCG-loaded BSG and dual response release systems for hydrogen peroxide and glucose

EGCG [19], a catechin found mainly in green tea, has good antioxidant and anti-inflammatory properties but is poorly absorbed after oral treatment. Therefore, we chose EGCG as a model cargo to achieve a conditioned controlled release and efficient delivery of the material to modulate inflammation. In particular, EGCG is loaded by physical adsorption into the voids of the mesoporous borosilicate glass, which PVA then encapsulates to prevent the excessive release of EGCG. In addition, introducing the borate base gives the material a selective release of hydrogen peroxide and glucose.

Firstly, borosilicate glass was prepared using the classical cetyltrimethylammonium bromide (CTAB) templated, alkali-catalyzed sol-gel method. Next, 3-Aminopropyltriethoxysilane (APTES), Carboxyl phenyl boric acid (PBA) and polyethylene glycol (PVA) were progressively added. Through a series of reactions, phenylboronic acid was gradually introduced to the surface of borosilicate glass. This phenylboronic acid then underwent a substitution reaction with the *cis*-diol structure on polyethylene glycol to form a reversible phenyl borate structure, giving rise to the intended ABBSG(PVA-PBA-BSG). Then, ABBSGs were observed by transmission electron microscopy (TEM). Following PVA wrapping, the 400 nm spherical borosilicate glass surface can be seen to have a 10 nm thickness of PVA, with the surface going from rough to smooth (Fig. 2A). Thermogravimetric analysis (TGA) was used to quantify this process, showing the formation of a 4.22% PVA cap on the BSG surface (Fig. S2B). The PVA cap, as anticipated, drastically reduced pore size from 3.4 nm to 0 nm, showing that the cargo could be properly enclosed in these voids (Fig. 2E). In addition to TEM, we analyzed the elemental composition by energetic-dispersive X-ray spectroscopy (EDS). The clear signals of Si, Ca, B, P, and C indicate the presence of borosilicate glass and PVA in ABNBSGs (Fig. 2B). More details on the chemical make-up of ABNBSGs are revealed via infrared spectra (IR). The expected characteristic peaks of the functional groups of ABBSGs in the synthesis stage, including the amino on the surface of BSG, are visible in infrared spectra. The characteristic peak at 1503

cm^{-1} is the bending vibration peak of amino group, while the absorption peak at 2930 cm^{-1} is attributed to the stretching vibration of the –CH$_2$-group (Fig. 1C). UV–Vis spectral analysis revealed the presence of an absorption peak at 252 nm, confirming the successful modification of the carboxyphenylboronic acid molecule (Fig. 2D). Then solid-state NMR was used to confirm that the alteration of PVA was successful (Fig. 2G). The above results indicate that PVA was successfully modified onto the surface of BSG.

When BSG is subjected to high sugar or hydrogen peroxide, the phenylboronic acid on the BSG surface can reversibly substitute with the *o*-dihydroxy group on the glucose. Furthermore, PVA and phenylboronic acid's ester link can be directly broken by hydrogen peroxide. Both may result in an increase in swelling or partial dislodgement between PVA and BSG, which will trigger the release of EGCG. The release of BSA from ABBSG was monitored by absorbance, and the finding revealed that the rate of BSA release increased with the addition of glucose and H$_2$O$_2$

(Fig. S2C). The loading efficiency of EGCG reached 87.56%, showing the excellent loading capacity of ABBSG for EGCG (Fig. S6).

3.2. Scaffold characterization

The changes in the swelling rate and PH of the scaffolds were examined by immersing the scaffolds in simulated body fluids (Figs. S1C–D). According to the findings, the addition of ABBSG further improved the densification of the hydrogel and decreased the swelling rate of the silk protein. The PH assay finding revealed that the PH of pure BSG was kept at an alkaline level but was kept at around 7.2 after being added to the silk scaffold. After the glass surface has been coated with PVA, the pH increases to 7.4 and is likely caused by the glass's breakdown being slowed down.

The compressive strength of the scaffold containing ABBSG was then tested by a mechanical testing machine. The results revealed that the
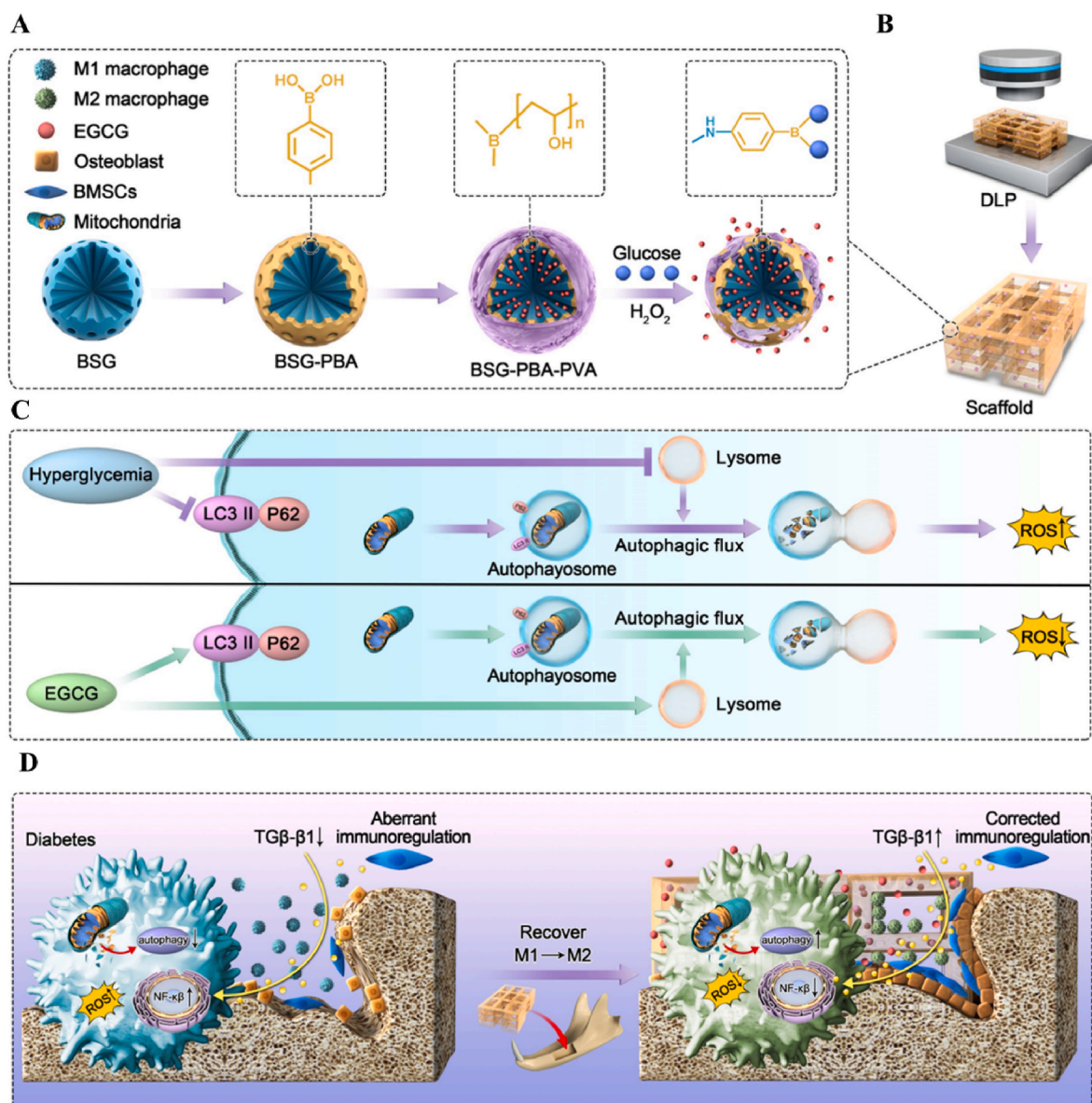

Fig. 1. Schematic illustration of ABBSG@EGCG fabrication by functional Borosilicate bioactive glass and epigallocatechin gallate for healing of alveolar bone defects in diabetes.

(**A**) Preparation of ABBSG through modification of BSG by Carboxyl phenyl boric acid (PBA) and polyethylene glycol (PVA). (**B**) ABBSG silk protein scaffold was built by DLP molding. (**C**) The ROS was reduced by enhancing macrophage autophagy and restoring autophagic flow. (**D**) ABBSG@EGCG promotes alveolar bone healing by lowering macrophage NF-κb activation and restoring immune regulation of mesenchymal stem cells in diabetes.
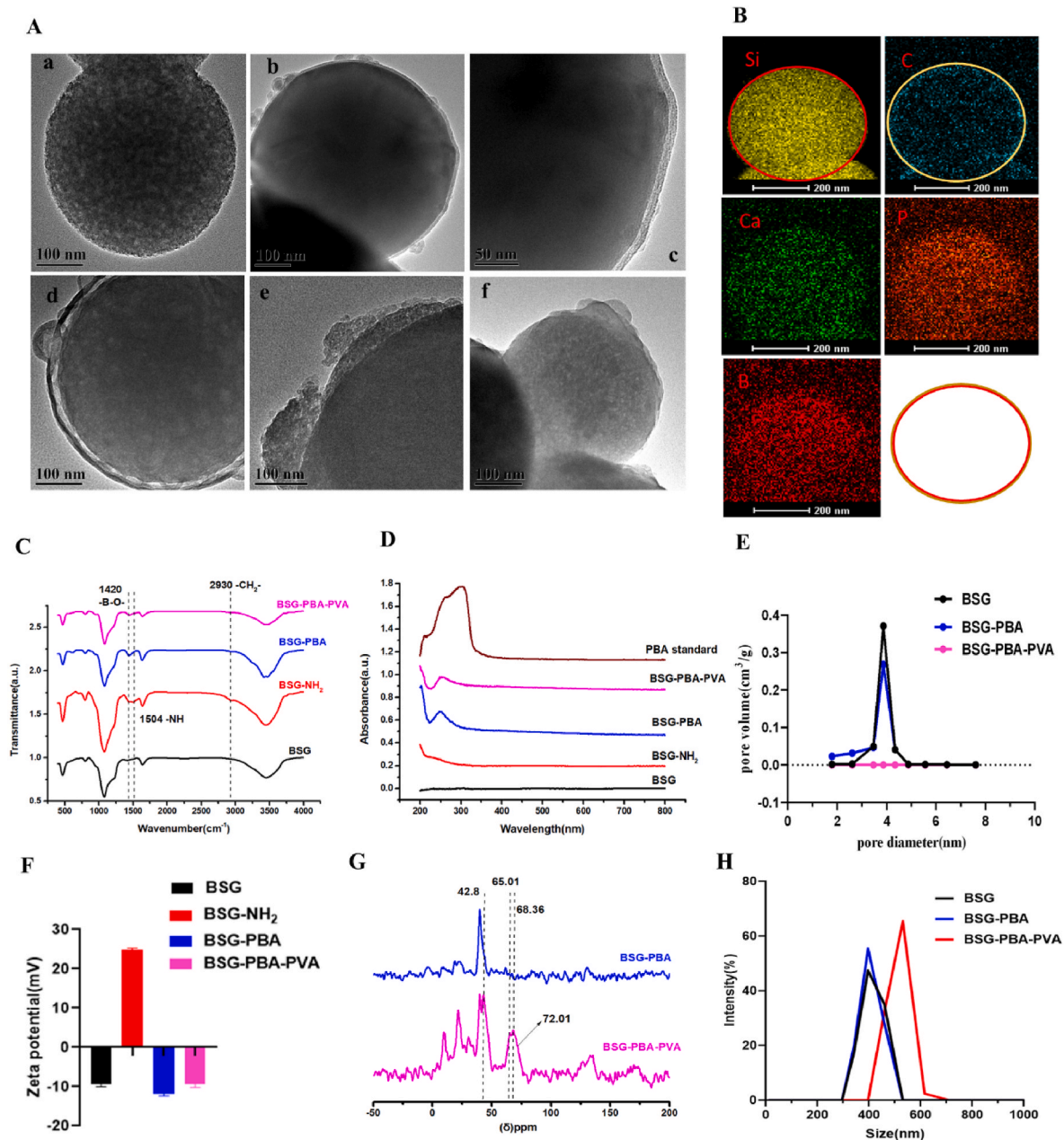
Fig. 2. Construction and characterization of ABBSG (BSG-PBA-PVA).
(**A**)Representative SEM image of ABBSG. ((a) Bare BSG, (b–c) ABBSG, (d) ABBSG@EGCG (EGCG loading), (e) ABBSG was soaked in glucose solution for 24h. (f) ABBSG was soaked in hydrogen peroxide solution for 24h.) (**B**) Element Mapping of ABBSG. Scale bar,200 nm. (**C**) Infrared spectra reveal the well-defined chemical composition of the ABBSG during each step in its formation. (**D**) UV–visible absorption spectra of BSG, BSG-PBA, BSG-PBA-PVA and PBA. (**E**) Pore-size distribution of BSG, BSG-PBA, and BSG-PBA-PVA. (**F**) Zeta potential of ABBSG after each step of functionalization to form ABBSG. (**G**) ^{1}H NMR spectra of BSG-PBA and BSG-PBA-PVA. (**H**) Size distribution of BSG, BSG-PBA, and BSG-PBA-PVA by DLS.

addition of ABBSG improved the mechanical strength of the scaffolds and that the maximum compressive strength could reach 400 kPa. The likely reason is that ABBSG acts as a physical filling for the hydrogel network, which increases the hydrogel's compressive properties (Fig. S1E).

The release of ions from the ABBSG scaffold was tested by ICP-OES (Figs. S1F–H) and showed a stable release of SiO_4^{4-}, BO_3^{3-}, Ca^{2+} ions and a slower release of ions from the PVA-coated BSG, which contributed to maintain the therapeutic effect.

3.3. EGCG inhibits the proinflammatory phenotype shift of macrophages under high glucose conditions

In diabetes, macrophage polarization favors pro-inflammatory M1

over anti-inflammatory M2 polarization. In our study, the western blot analysis of Raw 264.7 macrophages cultured under high glucose conditions showed considerably higher protein levels of M1 macrophage biomarkers for CD86 and iNOS than the control. Protein expression of CD206 and ARG, biomarkers of the associated M2 phenotype, was significantly reduced (Fig. 3A–B). Consistent with the polarization of macrophages towards the M1 phenotype, the expression of mRNA for inflammatory factors (IL-1, Il-6, TNF-a) released by macrophages under high glucose conditions was also significantly higher than that of controls (Fig. 3C). In contrast, when EGCG was added, the protein expression of CD86 and iNOS and the mRNA of the associated inflammatory factors were reduced. The protein expression of CD206 and ARG and the mRNA levels of related anti-inflammatory factors were significantly upregulated. Subsequently,
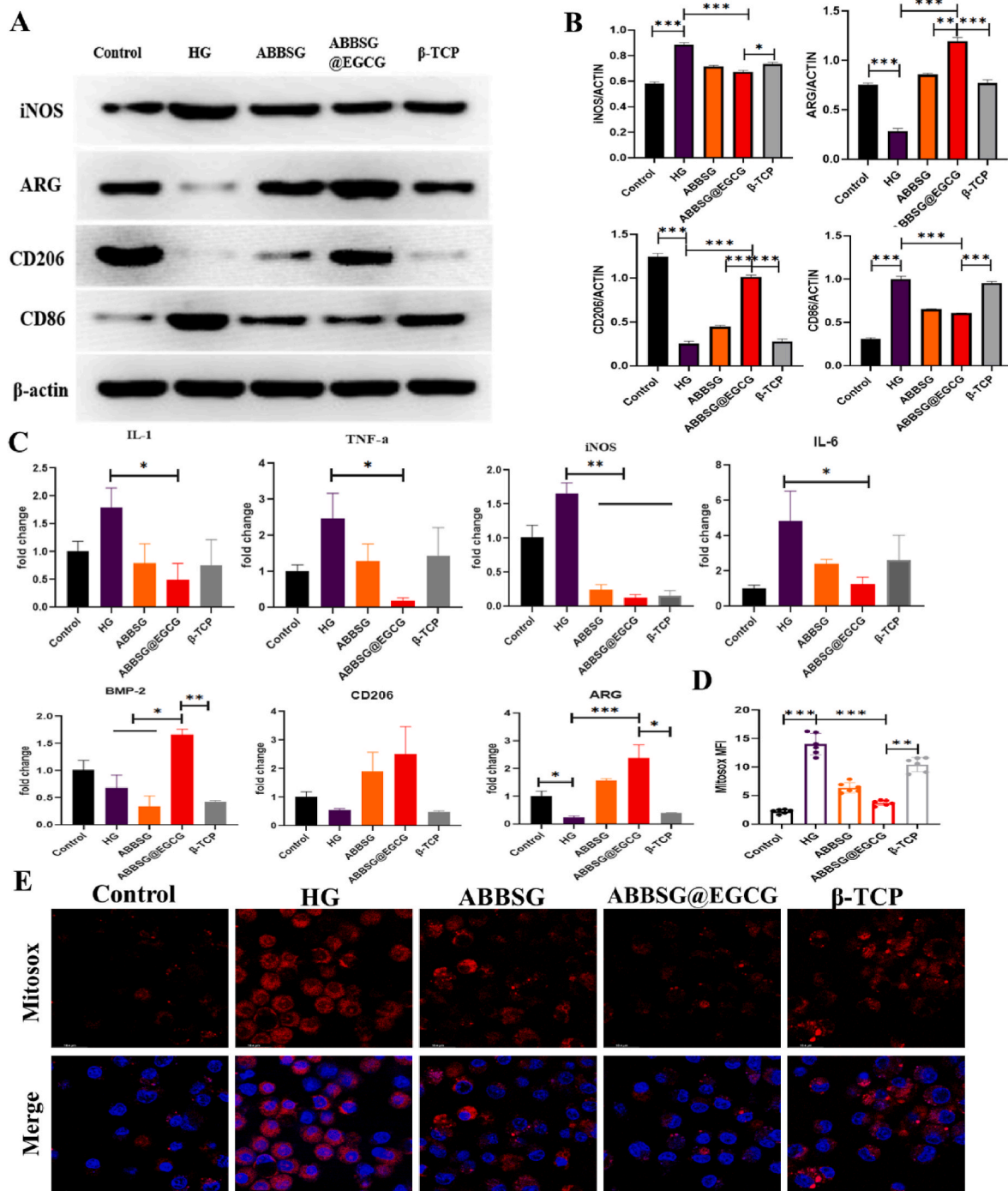
Fig. 3. ABBSG@EGCG inhibits the proinflammatory phenotype shift of macrophages under high glucose conditions.
RAW264.7 macrophages were induced under high glucose conditions for 3 days and continued to be cultured for three days after the addition of the material extract. The phenotype was characterized by Western blot. (**A-B**) Representative images of WB and quantitative analyses of iNOS-1, ARG, CD86 and CD206 (n = 3). (**C**) Expression of pro-inflammatory genes (TNF-a, IL-1, iNOS, and IL-6) and anti-inflammatory genes (arginase (arg), BMP-2, and CD206) were determined by qPCR (n = 3). (**D-E**) Mitochondrial reactive oxygen species were measured by Mitosox and cells were imaged via confocal microscopy. Scale bare: 10 μm. All results are representative of the data generated in at least three independent experiments and are presented as means ± SD. *P < 0.05, **P < 0.01, ***P < 0.001 by one-way ANOVA.

we counted the number and polarization type of macrophages surrounding the material at different time points. Immunofluorescence was carried out to quantify proinflammatory macrophage (M1) as F4/80$^+$ CD86$^+$ cells and alternatively activated macrophages (M2) as F4/80$^+$ CD206$^+$ Cells (Fig. 8A–B). In comparison to the β-TCP group, the number of M1 macrophages was significantly higher in the ABBSG and ABBS-G@EGCG groups 1 week after the scaffold was implanted; however, at 4

and 8 weeks, it was significantly lower in the ABBSG and ABBSG@EGCG group, and ABBSG@EGCG group had the fewest M1 macrophages. In contrast, the M2 macrophage in ABBSG@EGCG demonstrated a considerable rise after 4 and 8 weeks of scaffold implantation (Fig. 8C–E). These results demonstrate that the encouraging of M1 macrophage differentiation and the inhibition of M2 macrophage activation by diabetes are significantly modified by EGCG. Similar results, which also appeared in

the study by Qu et al. [20,21].

3.4. EGCG restores mitochondrial function, reduces mitochondrial ROS and inhibits NF-κb pathway activation under a diabetic condition

Diabetes-induced mitochondrial dysfunction in macrophages manifests abnormal mitochondrial dynamics, increased ROS, and decreased membrane potential. To determine the impact of EGCG on mitochondrial dysfunction in vitro, we cultured Raw264.7 cells in high glucose for 6 days (HG, 30 mM). The mitochondria in HG-treated cells were smaller, more punctate, and had significantly shorter lengths than those in controls, indicating that HG causes mitochondrial fragmentation (Fig. 4A–E). According to Western blot analysis, HG treatment dramatically raised the protein level of the mitochondrial fission protein dynamin-related protein 1 (DRP-1). However, the expression of the mitochondrial fusion protein mitofusin-2 (MFN2) (Fig. 5E) and the potential of the mitochondrial membrane reduced (Fig. 4F–G). The addition of EGCG significantly corrected the functional abnormalities of the mitochondria by decreasing the expression of DRP-1 and increasing the expression of the MFN2 protein. Similarly, the morphology of the mitochondria gradually changed after the addition of EGCG, from a punctate to a rod-like structure, and other mitochondrial parameters (Mitochondrial mass, Branch per Mito, Branch Length per Mito, Branch junction per Mito) were close to those of the control group. Simultaneously, The RAW264.7 macrophage membrane potential was increased. According to the findings, EGCG alleviated mitochondrial dysfunction due to high glucose and reduced the expression of ROS in mitochondria.

NF-κb is one of the key pathways in the controlling of macrophage phenotype. Phosphorylation of p65, a critical step in the NF-κb signaling cascade and a need for nuclear translocation and subsequent transcriptional activation, is a component of the traditional NF-κb, which is made up of p65 and p50. Numerous factors, include reactive oxygen species and cytokines such as (TNF-α and Il-β), could cause NF-κb to become active. Although the relationship between ROS and NF-κb is complex, it is generally accepted that extracellular reactive oxygen species suppress NF-κb activation and reduce NF-κb-mediated inflammatory signaling. In contrast, multiple investigations have demonstrated that mitochondrial ROS can support NF-κb activation. The possible reason for this is that ROS increase the phosphorylation of Iκb, triggering its degradation and allowing NF-κb to enter the nucleus. According to our research, HG-treated macrophages exhibited an increased proportion of p-65 protein entry into the nucleus, as well as increased protein expression of p-Iκb and P-p65 compared to the control group (Fig. 5A–D). This indicates that NF-κb pathway was turned on by the long-term HG condition. The addition of EGCG, however, resulted in decrease in the proportion of NF-κb entering the nucleus, as well as p-Iκb and P-p65 protein expression. The data above indicate that EGCG can counteract the activation of NF-κb in macrophages caused by high glucose. Its potential cause is the removal of ROS in mitochondria by EGCG.
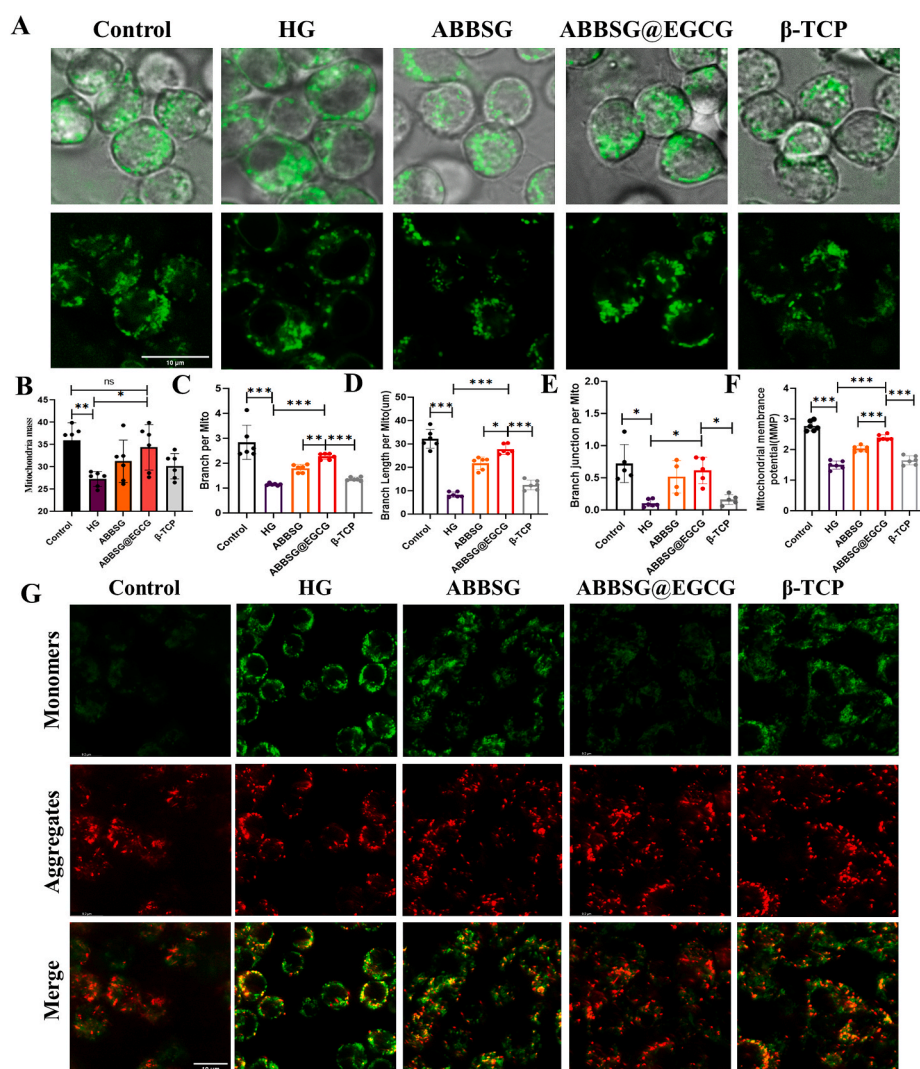

Fig. 4. Alteration of mitochondrial structure in macrophages induced by high glucose by ABBSG@EGCG.

(**A-E**) Representative immunofluorescence, loaded with Mito-green, and quantify of mitochondrial morphology in RAW 264.7 cells (n = 6). Scale bare: 10 μm. (**F-G**) The mitochondrial membrane potential was measured by JC-1(37 °C for 30min), and cells were imaged via confocal microscopy (n = 6). Scale bare: 10 μm. All results are representative of the data generated in at least three independent experiments and are presented as means ± SD. *P < 0.05, **P < 0.01, ***P < 0.001 by one-way ANOVA.
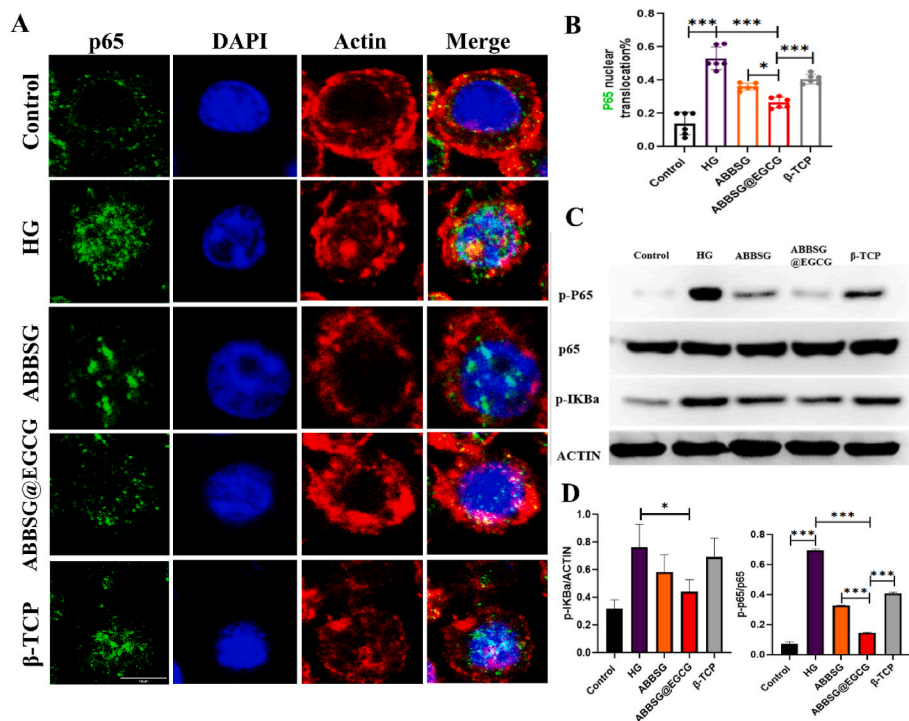
3.5. EGCG regulates autophagic flow in macrophage under diabetic conditions

Autophagy can selectively remove unnecessary organelles like damaged mitochondria, specifically mitochondrial autophagy. This process is an essential part of the immune cell and is involved in the subsequent immune response and the control of the overall quality of the mitochondria. It is generally recognized that sustained high glucose can cause mitochondrial damage. The damaged mitochondria, if not eliminated, can further lead to the accumulation of ROS-overproducing mitochondria, which in turn can exacerbate abnormal cellular function. Previous studies have confirmed that chronic high glucose conditions lead to the inhibition of mitochondrial autophagy in macrophages. In our study, the expression of microtubule-associated protein 1 light chain 3 II (LC3II) decreased after 6d of culture compared to the control group, whereas the expression of SQSTM1 (P62) increased, suggesting that not only was the level of autophagy inhibited but also the clearance of autophagosomes was impaired in macrophages under prolonged high glucose conditions (Fig. 6E). We, therefore, measured the autophagic process using a tandem fluorescent RFP-GFP-LC3 reporter system. Autophagosome accumulation is indicated by RFP (red) and autophagosome abundance is indicated by double fluorescence (RFP-GFP; yellow). Under high glucose conditions, we observed an increase in the number and co-localization of yellow dots in macrophages (Fig. 6D). Comparatively to ABBSG and β-TCP, the addition of EGCG increased the expression of LC3 II more noticeably while decreasing the expression of P62. Meanwhile, we found that the expression of LC3II increased over time in animal experiments. At 1w, the MFI of β-TCP was higher than the other two groups, but at both 4 and 8 weeks it showed a higher MFI of ABBSG@EGCG than the other groups (Fig. 8F–G). In addition, the RFP-GFP-LC3 reporter system also showed that the number of yellow dots of double fluorescence decreased after EGCG addition (Fig. 6C). The data mentioned above imply that lysosomal function and autophagic flux may be recovered by EGCG.

Subsequently, autophagy levels were further observed by transmission electron microscopy (Fig. 6A). In agreement with the results of the RFP-GFP-LC3 reporter experiment, the number of autophagic vesicles in macrophages was drastically decreased under high glucose conditions. When EGCG-loaded BSG was added, the quantity of autophagic vesicles recovered greatly in comparison to the other groups (Fig. 6B).

3.6. EGCG restores clearance of damaged mitochondria

When mitochondrial damage occurs, the proteins necessary to recruit damaged mitochondria to the autophagosome include PTEN-induced putative kinase 1 (PINK1) and PARKIN, which should be elevated. However, following 6 days of incubation in a high glucose environment, protein expression of PINK1 and PARKIN reduced (Fig. 7E). This suggested that HG prevented mitochondrial autophagy from forming. We subsequently found that high glucose reduced the co-localization of Mito-red with LC3 and increased the co-localization of Mito-red with Lyso-Green in RAW264.7 macrophages (Fig. 7A–B). In contrast, EGCG significantly increased the co-localization of Mito-red and LC3 and decreased the co-localization of Mito-red and Lyso-green with higher levels of PINK1 and Parkin expression. These findings imply that decreased clearance of damaged mitochondria, which results in increased ROS generation, is most likely the cause of macrophage mitochondrial dysfunction in diabetes. When EGCG was administered, the expression of the mitochondrial autophagy recruitment protein rose, along with the co-localization of LC3 with Mito-red increasing and Lyso-green and Mito-red decreasing, further demonstrating the restoration of mitochondrial autophagy flow (Fig. 7C–D).

3.7. EGCG boosts the number of stem cells and reduces mitochondrial ROS levels under high glucose conditions

The number of bone marrow mesenchymal stem cells plays a crucial role in limiting inflammation during the healing process of bone defect wounds; however, in diabetes, this process is adversely interrupted. Therefore, we first looked at the effect of EGCG on stem cell numbers under high glucose conditions through apoptosis assays, CCK8 assays and EdU cell proliferation assay. The findings demonstrated that high glucose circumstances enhanced stem cell death (Fig. 10F) and lowered
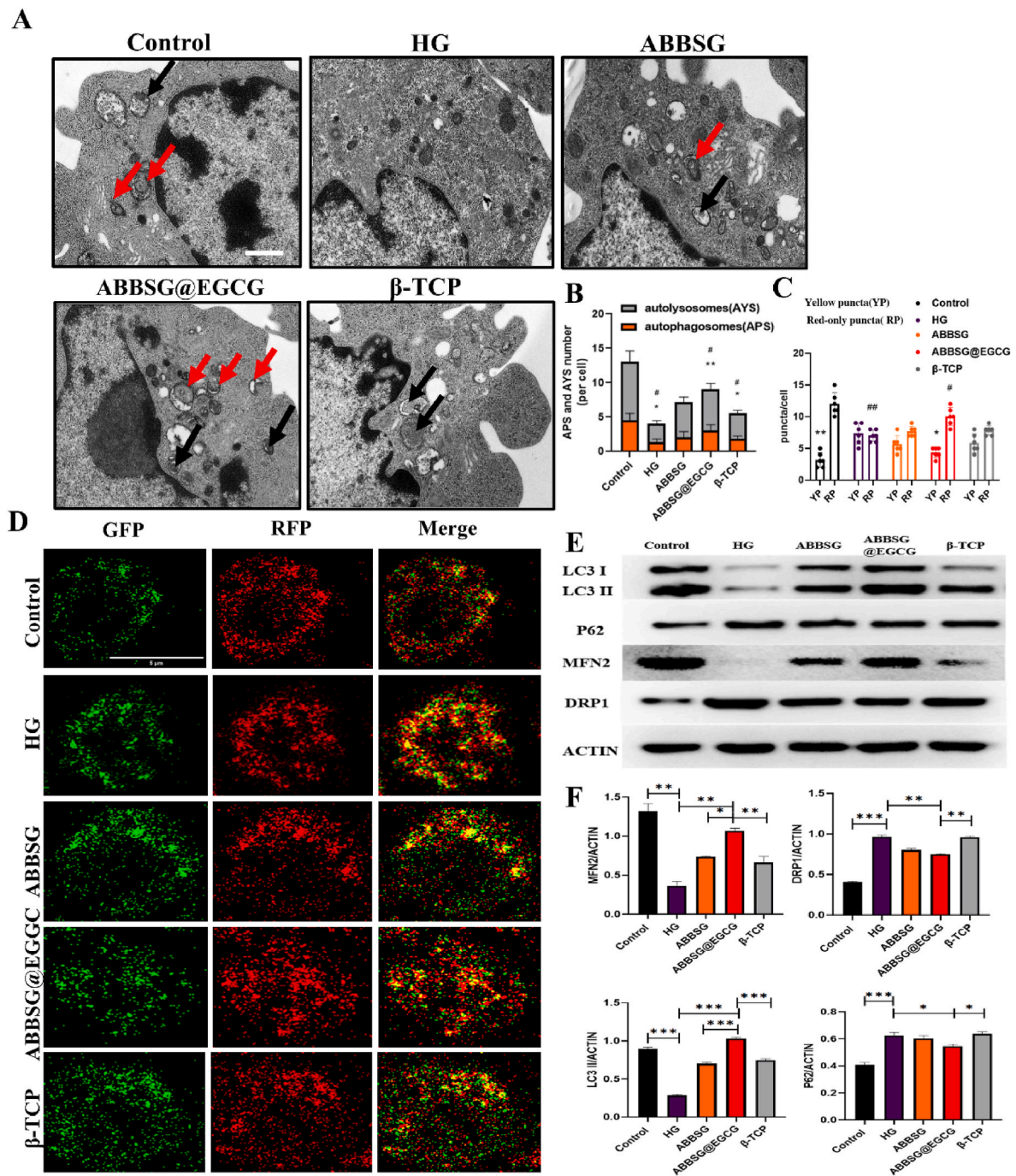
Fig. 6. ABBSG@EGCG regulates autophagic flow in macrophage under diabetic conditions.
(**A-B**) TEM analysis of RAW264.7 and quantify of autolysosomes (AYS) and autophagosomes (APS) under different conditions (n = 3). Scale bare: 500 nm. (**C-D**) Differentiated RAW264.7 cells were transduced with GFP-RFP-LC3 adenovirus for 24 h followed by exposure to different conditions, and cells were imaged via confocal microscopy (n = 6). Scale bars: 10 μm. (**E-F**) Representative images of WB and quantitative analyses of LC3, P62, DRP1, and MFN2 (n = 3). All results are representative of the data generated in at least three independent experiments and are presented as means ± SD. *P < 0.05, **P < 0.01, ***P < 0.001 by one-way ANOVA.

stem cell growth rates (Fig. 9G, S4). The ABBSG group outperformed the β-TCP group even though there was no statistically significant difference between the two groups. Subsequently, we specifically targeted MSC markers CD90 and Sca1 with an antibody immunofluorescence assay to assess the effect of the scaffold on MSC numbers (Fig. 10A). The number of MSCs increased gradually in all groups, however, the increase in MSCs was more evident in the EGCG group compared to the β-TCP group (Fig. 10C–D).

Then, we observed the effect of EGCG on mitochondria and ROS in

stem cells under high glucose conditions. Mito-sox red was used to color-code mitochondrial ROS. Confocal graphs showed a significant increase in red fluorescence intensity in the mitochondria of mBMSCs in the HG group compared to the control group. The addition of the material decreased the red fluorescence intensity to varying degrees, but the decrease was most pronounced in the group containing EGCG (Fig. 9A). Consistent with the results observed for mitochondrial reactive oxygen species, confocal microscopy showed that the mitochondrial length of stem cells in the high glucose condition was significantly shorter, and all
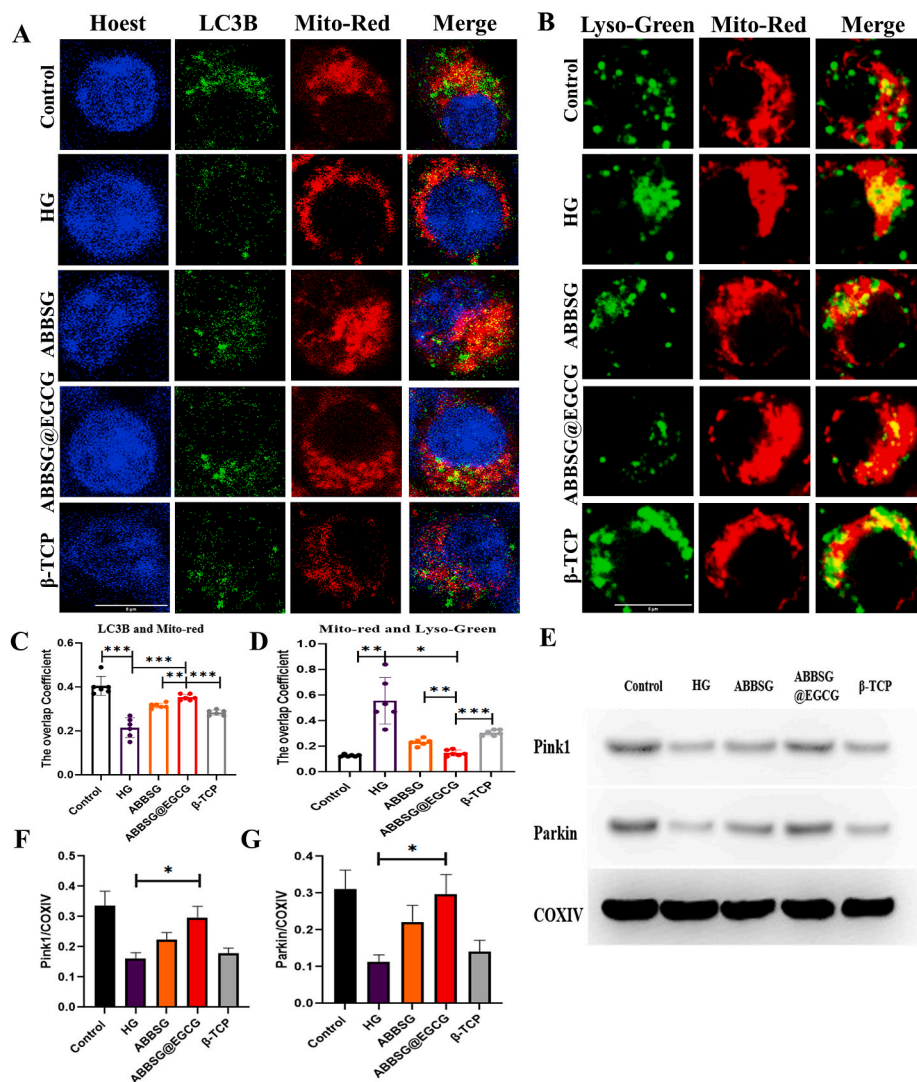
Fig. 7. ABBSG@ EGCG promotes impaired mitochondrial clearance in RAW264.7 cells
(**A-D**) Co-localization of mitochondria with autophagosome marker LC3B or Lysotracker-green in HG-induced RAW 264.7 cells, cells were imaged via confocal microscopy (n = 6). Scale bars: 10 μm. (**E-G**) Representative images of western blot and quantitative analyses of PINK1 and Parkin (n = 3). All results are representative of the data generated in at least three independent experiments and are presented as means ± SD. *P < 0.05, **P < 0.01, ***P < 0.001 by one-way ANOVA.

other parameters were lower than in the control group (Fig. 9E). Meanwhile, the membrane potential of stem cell mitochondria also appears to be reduced. When EGCG was added, the fluorescence intensity of mitochondrial ROS in stem cells was significantly reduced, and the mitochondrial membrane potential was restored. In addition, mitochondrial fragmentation and all other parameters improved compared to the HG group. The above results indicate that EGCG improved stem cell mitochondrial dysfunction, reduced ROS levels, and increased stem cell numbers under high glucose conditions.

3.8. EGCG down-regulates the NF-κb pathway in stem cells and restores immunomodulatory functions

To find potential mechanisms by which EGCG regulates the immunomodulatory function of stem cells, we examined the expression of NF-κb in stem cells. Diabetes can impair the ability of stem cells to express TGF-β1 and induce M1 macrophage formation through aberrant activation of NF-κb in the periosteum. Under the observation of a confocal microscope, the nucleus is blue, and the p65 protein is green. In the control group, p65 is in the cytoplasm; however, the p65 protein is transferred to the nucleus following prolonged high glucose stimulation. When the material was added, the nuclear transfer of p65 was reduced, with the ABBSG@EGCG group having the least nuclear transfer of p65. Similarly, the western blot showed a significant decrease in protein expression of p-p65 in the ABBSG@EGCG group compared to the high

glucose group (Fig. 9B–C). The above results suggest that the addition of EGCG inhibited the activation of the NF-κb pathway in MSCs.

Then we examined the expression of TGF-β1, a cytokine known to regulate M1/M2 homeostasis. High glucose reduced secretion of TGF-β in BMSCs compared to the control group (Fig. 9F). In contrast, the release of TGF-β was somewhat restored in the ABBSG@EGCG group, while the release of ABBSG and β-TCP did not differ statistically from the high glucose group. The above results suggest that the restoration of stem cell immunomodulatory capacity by EGCG is likely to be achieved by down-regulating the activation of the NF-κb pathway and increasing the expression of TGF-β. Meanwhile, the results of animal experiments showed that the expression of TGF-β in the ABBSG@EGCG group was higher than that in the ABBSG and β-TCP groups 4 weeks after scaffold implantation. Although the expression of TGF-β decreased overall after 8 weeks, it still maintained the original trend (Fig. 10B, E).

3.9. Micro-computed tomography (micro-CT) analysis of the periodontal bone resorption

To evaluate EGCG-loaded borosilicate glass-photosensitive filamentous protein scaffolds in vivo, we explored their efficacy in the bone repair of mandibular defects in STZ-induced diabetic rats. Eight-week-old SD rats were injected intraperitoneally with 40 mg/kg STZ to establish a diabetic rat model and then reared for 8 weeks. A 2*5*2 mm alveolar bone defect was prepared on the buccal side of the mandible,
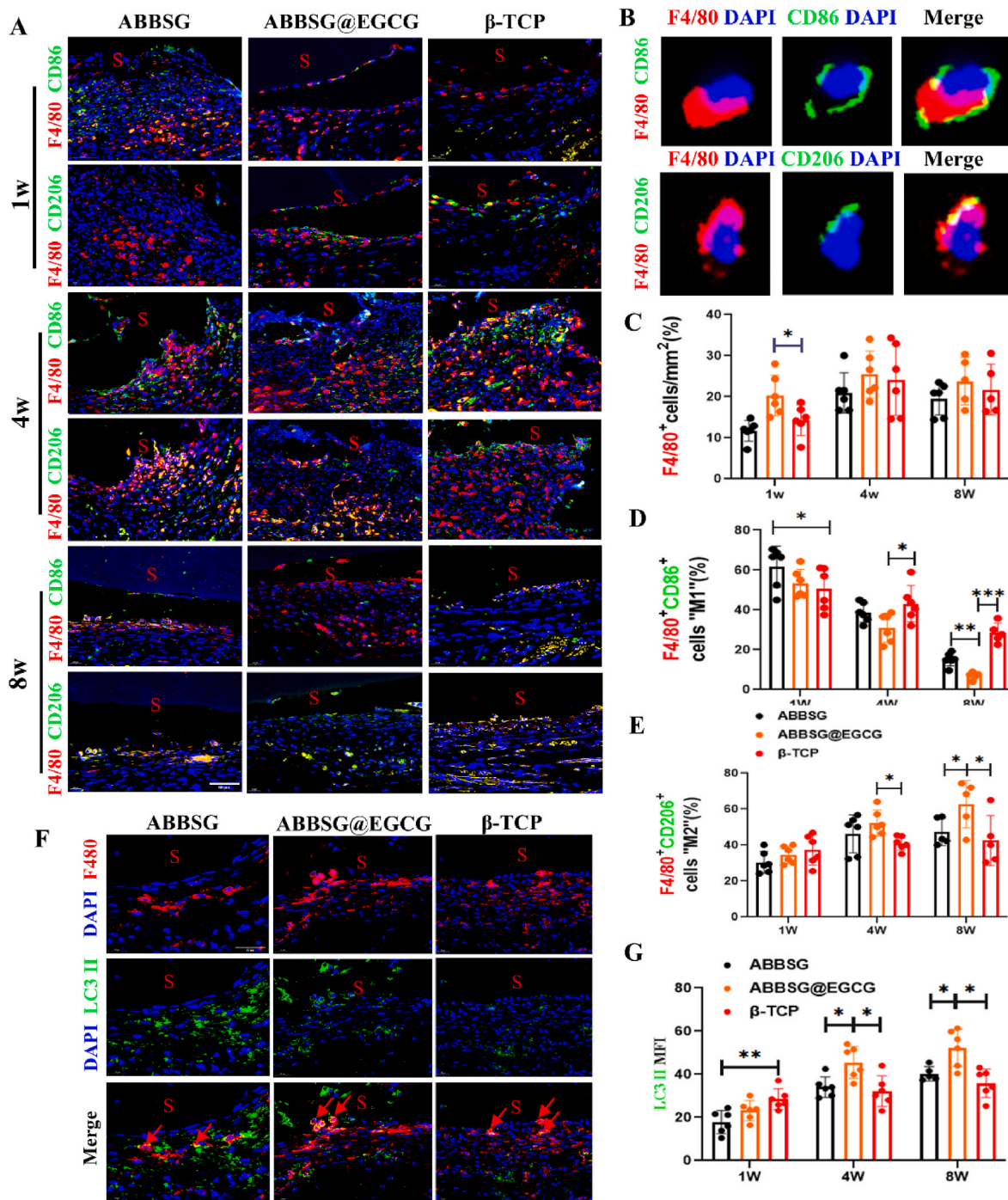
Fig. 8. ABBSG@EGCG accelerates recovery of macrophage phenotypic transformation in a diabetic alveolar bone defect model
(**A**) Double immunofluorescence to detect M1 (F4/80$^+$CD86$^+$) and M2 (F4/80$^+$CD206$^+$) macrophages in a diabetic alveolar bone defect model. Scale bars, 50 μm. (**B**) Representative images show M1 and M2 macrophages. Scale bare: 20 μm (**C-E**) Quantification of M1-and M2-immunopositive cells per total nucleated cells after scaffold implated 1w, 4w and 8w, as determined by immunofluorescence(n = 6). (**F-G**) Immunofluorescence analysis of LC3 II (green) in macrophages (red) (n = 6). All results are representative of the data generated in six independent experiments and are presented as means ± SD. *P < 0.05, **P < 0.01, ***P < 0.001 by one-way ANOVA.

and the scaffold was subsequently implanted. Compared to the β-TCP group (BV/TV% = 18.75), the BV/TV values increased to 21.03 and 27.04 in the ABBSG and ABBSG@EGCG groups, respectively, confirming the positive role of BSG in promoting alveolar bone repair and the further enhancement of the restorative effect by EGCG (Fig. 11C). Combined with the other two parameters, the ABBSG@EGCG group showed the most favorable results compared to the other groups. The trabecular separation (Tb. Sp) represents the average distance between

trabeculae. As shown in Fig. 11, the Sp value of ABBSG@EGCG (0.69 mm) was significantly lower than that β-TCP group, indicating a good treatment effect in the ABBSG@EGCG group. Although there was no significant difference between the ABBSG (1.19 mm) group and the β-TCP (1.56 mm) group, the ABBSG group was lower. The above results indicate that the combination of ABBSG @EGCG has a satisfied therapeutic effect in diabetic alveolar bone restoration.
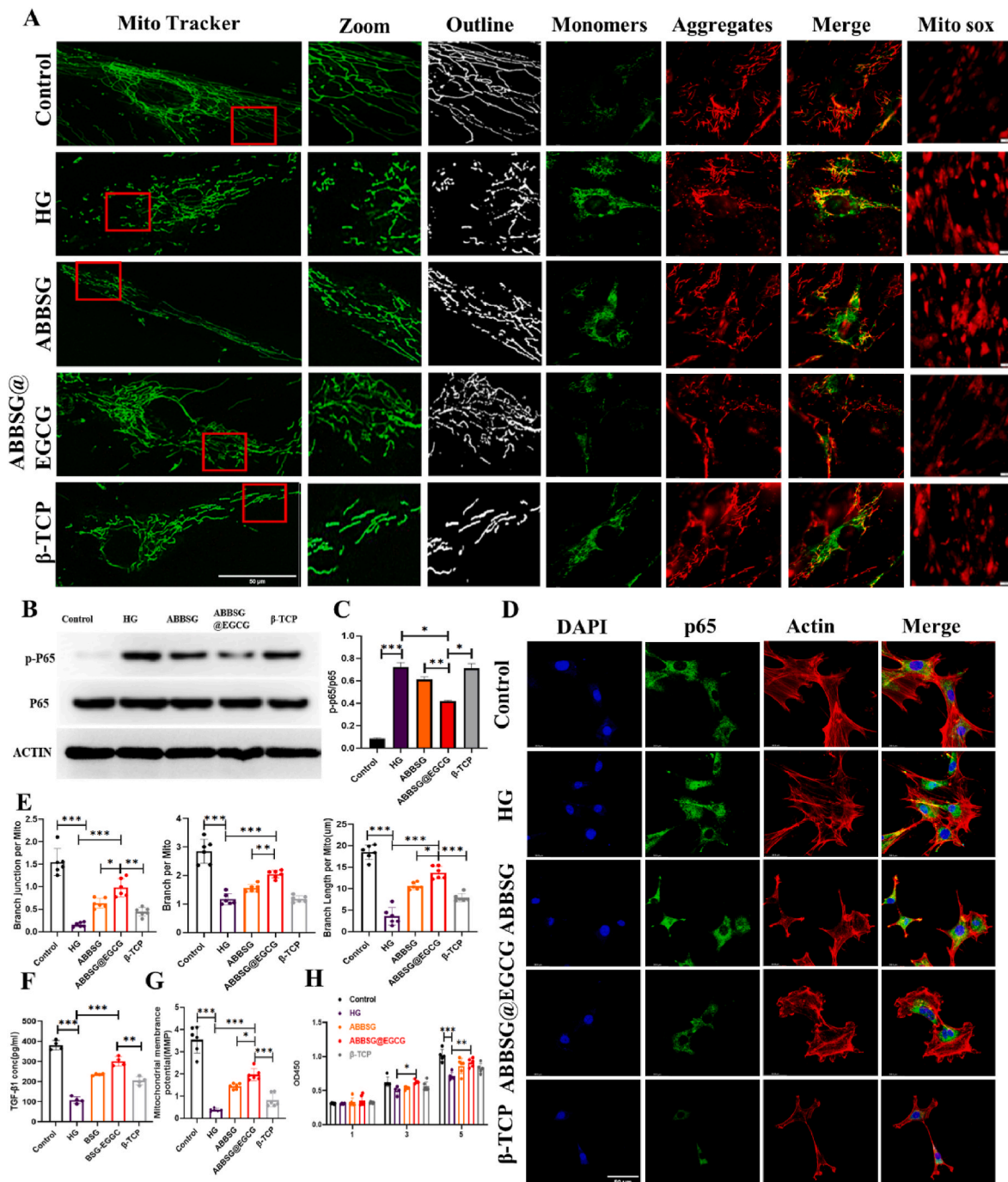
Fig. 9. Effect of ABBSG@EGCG on mitochondria and NF-κb of BMSCs under a diabetic condition.
The mBMSCs were treated with high glucose for 3d before being handled. (**A**) Representative immunofluorescence of mitochondria, the mitochondrial membrane potential and mitochondrial reactive oxygen species in mBMSCs. Scale bare:10 μm. (**B–C**) Representative images of western blot and quantitative analyses of p-p65 and p65 (n = 3). (**D**) Immunofluorescence with NF-κB antibody in mBMSCs under high-glucose (HG; 30 mmol/L) conditions. Scale bare:10 μm. (**E**) The quantify of mitochondrial morphology in mBMSCs (n = 6). (**F**) TGF-β1 concentration in mBMSCs, as determined by ELISA (n = 3). (**G**) Proliferation of mBMSCs after HG incubation for 1, 3 and 5 days. Quantified by cck8 kit. All results are representative of the data generated in at least three independent experiments and are presented as means ± SD. *P < 0.05, **P < 0.01, ***P < 0.001 by one-way ANOVA.

4. Discussion

Hyperglycemia is brought on by β cell death and insufficient glucose transporter 2 expression. Under hyperglycaemic conditions, activators of the polyol pathway, the aminoglycan pathway, and protein kinase C are hypothesized to boost oxidative stress and cause inflammation to last longer and produce more pro-inflammatory factors. Although there are many factors that might impair the repair of alveolar bone defects in

diabetics, oxidative stress has been recognized as a significant pathogenetic mechanism impeding the process and as a major source of complications [22].

In the current study, we established the PBA-PVA system on mesoporous borosilicate glass, a structure with dual triggering behavior of glucose and reactive oxygen. BSG-PBA-PVA has good biocompatibility after complexation with photosensitive filipin proteins. *In vitro* drug release studies showed that the BSG-PBA-PVA structure, when combined
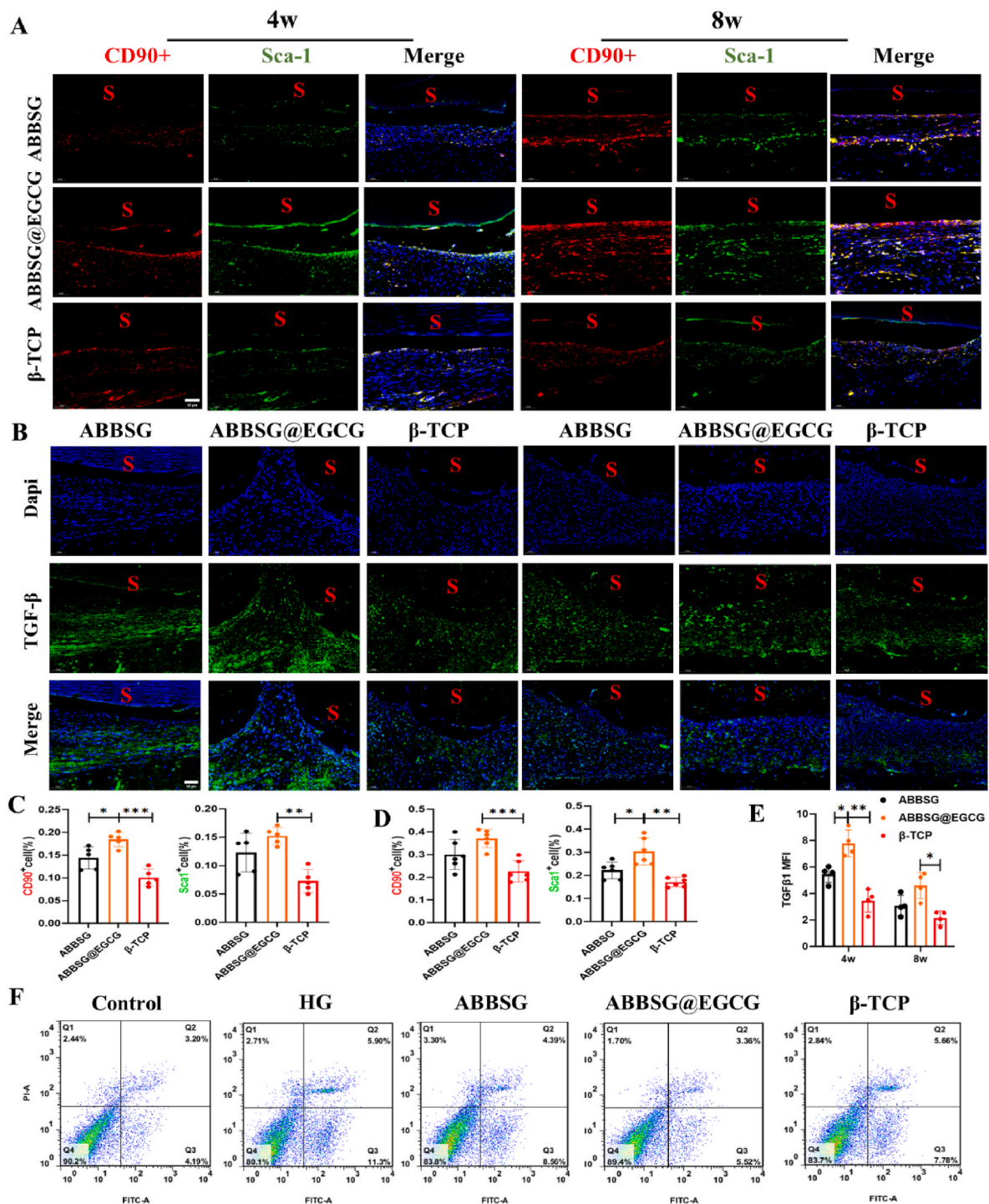
Fig. 10. ABBSG@EGCG significantly increased the number of mesenchymal stem cells
(**A**) Immunofluorescence of CD90 and Sca1 in 4W and 8W defects of diabetic mice. Representative images are shown, and the letter "S" represents the position of the scaffold. Scale bars, 50 mm. (**B**) Immunofluorescence with TGF-β1antibody in 4W and 8W defects of diabetic mice. Data are expressed as MFI (n = 6) (E). Scale bars, 50 mm. (C–D) Quantification of CD90 and Sca1 immunopositive cells per total nucleated cells in ABBSG, ABBSG@EGCG and β-TCP groups. Data from 4W to 8W defects were shown (n = 6). (**F**) Flow cytometry result with Annexin V-FITC/PI staining on different sample(n = 3). All results are representative of the data generated in at least three independent experiments and are presented as means ± SD. *P < 0.05, **P < 0.01, ***P < 0.001 by one-way ANOVA.

with glucose and H_2O_2, boosted the rate of BSA release. Subsequently, the scaffold was implanted into the alveolar bone defects in STZ-induced diabetic rats to verify the osteogenesis. After 8 weeks of implantation, in vivo test showed that ABBSG loaded with EGCG had larger BV/TV fractions and bone trabeculae than other groups, suggesting that the addition of EGCG increased the alveolar bone regeneration. Meanwhile, these findings were also supported by Goldner and safranin O staining

(Fig. 11G). Interestingly, the good bone-enhancing effect of EGCG was also found in the study by Qu et al. [23,24]. However, the possible reason why EGCG improves diabetic alveolar bone repair is unclear, thus we would like to discuss the potential mechanism.

It is common knowledge that mitochondria are the primary generator of reactive oxygen species (ROS) in macrophage. In vitro, high glucose induces an excess of ROS and reactive nitrogen species (RNS),
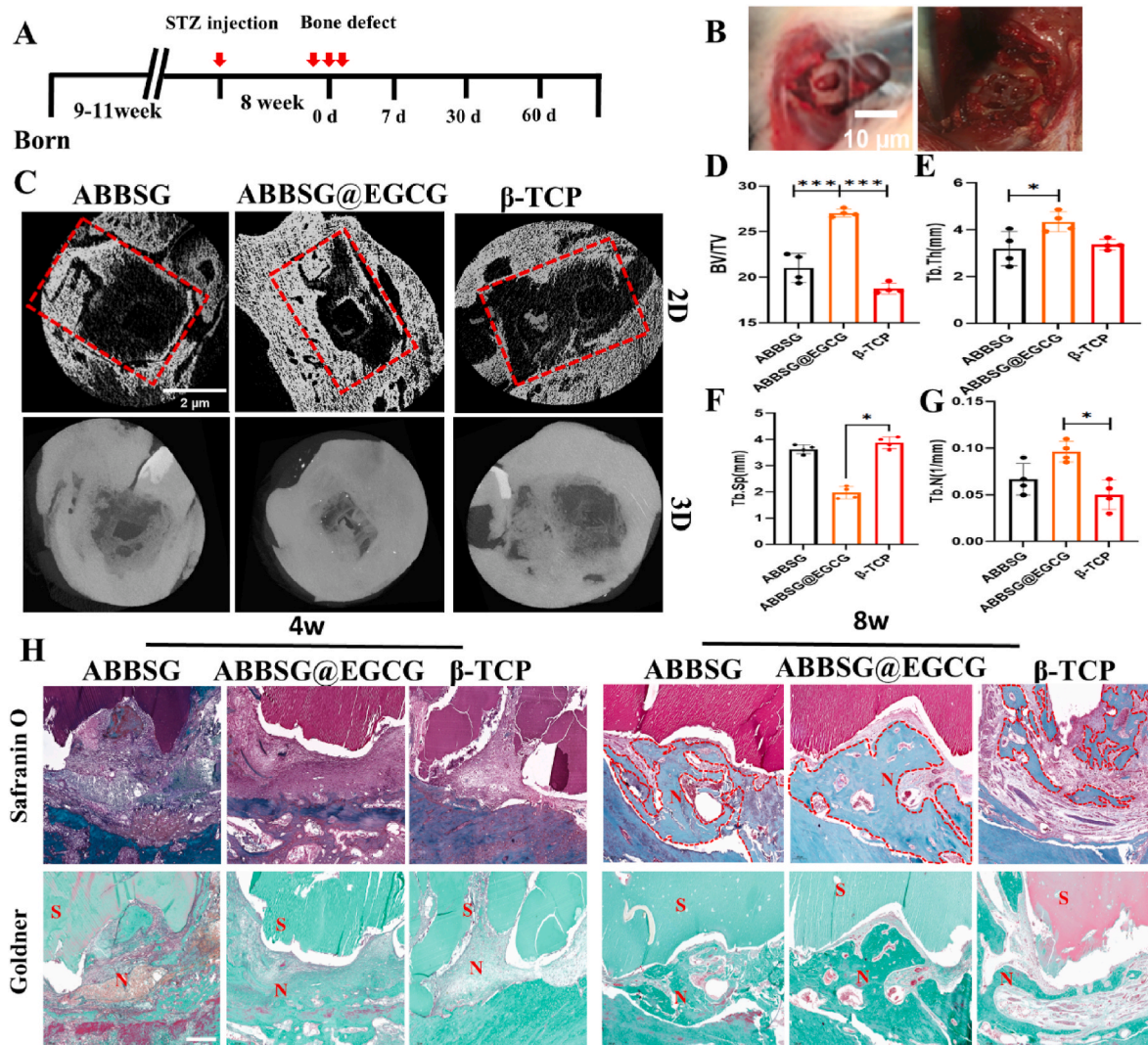
Fig. 11. Healing of alveolar bone defects in a diabetic rat model with ABBSG@EGCG
(**A**)Experimental design of ABBSG@EGCG silk protein scaffold implanted in a diabetic rat alveolar bone defect model. (B) Construction of alveolar bone defects and injection of scaffolds. (**C**) Representative Micro-CT images of maxillary alveolar bone after the treatment for 8w: the above image in each group displays the 2D reconstruction image and the images below represent the 3D reconstruction image. (**D-G**) The quantitative analysis of bone-related parameters: BV/TV(D), Tb.Th(E), Tb. Sp(F), and Tb.N(G) from micro-CT images (n = 4). (**H**) Safranin O and Fast Green staining and Goldner staining in 8W of diabetic rat model. Representative images are shown. Scale bars, 500 μm. All results are representative of the data generated in at least four independent experiments and are presented as means ± SD. *P < 0.05, **P < 0.01, ***P < 0.001 by one-way ANOVA.

which activates macrophages in a pro-inflammatory manner [25]. Mitochondria are highly dynamic organelles that maintain a balance of fission and fusion according to the metabolic demands of the cell. According to earlier research, diabetes increased DRP1 protein and phosphorylation, which in turn enhanced mitochondrial fission and ROS [26]. The overproduction of ROS is an important mechanism for the M1 phenotypic polarization of macrophages and the subsequent release of pro-inflammatory factors [27,28]. Our study found that the addition of EGCG could inhibit mitochondrial fission and thus improve the biological and histological features of diabetes by lowering DRP1 expression and raising MFN2 expression. Additionally, the ABBSG group outperformed the β-TCP group in terms of mitochondrial function recovery, possibly due to the antioxidant properties of boron itself. Relevant studies have confirmed that low doses of boron can inhibit apoptosis and improve the antioxidant system [29].

Autophagy plays an important role in maintaining the function of organelles such as mitochondria [30]. In order to keep the intracellular environment healthy and functioning properly, cells often need to constantly remove damaged proteins and organelles (such as

malfunctioning mitochondria from protracted oxidative stress [31]. However, autophagy blockade causes an accumulation of damaged, ROS-generating mitochondria, which activates the NLRP3-inflammasome and causes NF-κb-regulated inflammation. This suggests that the autophagic pathway can also be linked to pro-inflammatory signaling through the oxidative stress pathway [32–34]. Previous studies have shown that diabetes leads to elevated release of pro-inflammatory factors from M1 macrophages by disrupting mitochondrial function and impairing autophagosome clearance [35,36]. Impaired autophagic flux and inhibition of autophagosomes activation were manifested by a decrease in LC3 II synthesis protein and elevated expression of P62 protein, which is a key protein for assessing autophagic flux patency. Adding EGCG elevated the LC3II expression level while decreasing the P62. Furthermore, more LC3 protein puncta and autophagic vesicles were detected, demonstrating that EGCG could enhance autophagy in macrophages and alleviate the blockage of autophagic flow.

This study suggests that the direct modulation of the inflammatory phenotype of macrophages in the diabetic state by EGCG is likely to be associated with the release of the autophagic flow restricted by high

glucose. The release of autophagosome accumulation restores mitochondrial function, thereby reducing the production of ROS and activation of NF-κb. In other words, EGCG could more efficiently transform the inflammatory macrophage phenotype in a high-glucose environment. However, more macrophages were found in both the ABBSG and ABBSG@EGCG groups, and the proportion of M1 macrophages was higher than that in the β-TCP group at week 1. The possible reason for this is the abrupt release of ions from borosilicate glass in the early stages. In addition, we observed a relatively low proportion of M1-type macrophages in the EGCG-loaded group relative to the ABBSG group, which could be attributed to the damage caused by oxidative stress due to the sudden release of excessive borate ions. In contrast, EGCG reduced the oxidative stress damage caused by excess boric acid root, thus exhibiting lower M1 macrophages compared to the ABBSG group. It is well known that M0, M1 and M2 macrophages all promote osteogenesis, with M1 macrophages showing a largely positive role in the early stage [37]. Further studies have identified COX2/PEG2 as an important potential cause of mediating the osteoinductive communication between inflammatory macrophages and mesenchymal stem cells [38]. It follows that appropriate inflammatory macrophages may also be a contributor to accelerated alveolar bone formation. Furthermore, the remarkable up-regulation of the M2 macrophage ratio after 4 weeks also suggests that the ABBSG@EGCG group regulated the macrophage phenotype better than the β-TCP group. Thus, the timely transition of inflammatory phenotype to anti-inflammatory phenotype in macrophages is an important mechanism by which ABBSG@EGCG accelerates alveolar bone repair in diabetes.

The second major effect of diabetes on alveolar bone repair is the immunomodulatory capacity of bone marrow-derived stem cells (BMSCs). BMSCs have the ability to modulate the phenotypic balance of macrophages to reduce tissue inflammation. Both maxillary-derived MSCs and human gingival-derived MSCs were also found to have a role in regulating the inflammatory phenotype of macrophages [39,40]. However, diabetes often interferes with this resolution through abnormal NF-κb activation. Based on *Kang* et al., specific inhibition of NF-κb in MSCs by IKKb deletion reversed diabetes-enhanced apoptosis and reduced proliferation of MSCs [15]. Further studies revealed that homing and differentiation of MSCs is not a key mechanism for regulating inflammation. Instead, paracrine action may be the main mechanism by which MSCs are involved in tissue damage and repair [41]. We investigated the potential role of EGCG on MSCs in the healing of diabetic alveolar bone defects and found that it reduced the detrimental effects of high glucose on MSC expansion by inhibiting apoptosis and promoting proliferation. Although NF-κb usually has a direct anti-apoptotic effect [13], it has also been reported to promote apoptosis and inhibit proliferation under diabetic conditions [42]. This polarizing effect of NF-κb is likely related to the ROS-triggered degradation of the NF-κb inhibitor IκB [43]. We also found that the effect of EGCG on maintaining BMSC numbers is likely to be associated with disruption of activation of the aberrant NF-κb in the MSCs. Disruption of NF-κb activation is likely to be associated with improved mitochondrial function and reduced mitochondrial ROS by EGCG. In addition, inhibition of NF-κb activation restored production of TGF-β and increased the function of BMSCs in regulating the inflammatory phenotype of macrophages.

The important role of TGF-β in regulating inflammation and promoting bone regeneration has been well documented, especially when recombinant TGF-β1 was administered early in the fracture, and inflammation in the trauma was greatly reduced with the restoration of the M2 ratio [15]. Our study found that the expression of TGF-β was significantly higher in the ABBSG@EGCG and ABBSG groups 4 weeks after scaffold implantation. We speculate that the expression of TGF-β1 here is likely to be derived from M2 macrophages and BMSCs that restore immunomodulatory functions.

Activated TGF-β1 release in the microenvironment has different effects on osteoblasts that are context-, time- and dose-dependent [44]. Despite some contradictory findings, most experiments show that TGF-β promotes osteoblast proliferation and early differentiation of stem cells, while inhibiting late differentiation and matrix mineralization [45,46]. This may also explain the significant increase in the number of BMSCs in the group with high TGF-β expression at 4 Weeks. Conversely, at 8 weeks, the expression of TGF-β decreased in the ABBSG@EGCG and ABBSG groups with increasing osteogenesis (Fig. 10E.) . Consequently, we speculate that in addition to the regulation of inflammatory macrophages by the material, the immunomodulatory role of MSCs is likely to play a prominent role. Thus, inhibition of the activation of high glucose-enhanced NF-κb in MSCs is an essential mechanism for defusing inflammation.

Interestingly, we observed superior osteogenesis and inflammation control in ABBSG group compared to β-TCP group respectively on 4 and 8 Weeks. The reason may be attributed to the controlled release of B ions from ABBSG in spontaneous regulation of inflammation. A number of records indicate good antioxidant effects of boron ions, and thus believed that the antioxidant damage of boron is mainly by increasing the body's stores of glutathione and meanwhile inhibiting other reactive oxygen species [47]. Therefore, it can also be concluded that Ca ions alone hardly play a role in regulating inflammation to promote alveolar bone defect repair in diabetes. In this study, the incorporated EGCG acts as a more positive regulator of oxidative stress and inflammation in the early stage of implantation, while subsequent release of boron ions from ABBSG is a key factor in regulating bone remodeling in the mid to late stages.

In summary, the addition of EGCG to borosilicate bioglass in the diabetic setting resulted in a more significant modulation of the macrophage phenotype in a timely manner. The reason for this may be related to the fact that EGCG regulates the upregulation of NF-κb expression due to the overproduction of ROS. On the one hand, EGCG can directly regulate the polarization state of macrophages by restoring the mitochondrial autophagic flow in macrophages. In addition, EGCG can also indirectly regulate the phenotype of macrophages by restoring the immunomodulatory function of stem cells. The altered phenotype of macrophages reduces local inflammation and increases the restoration of diabetic alveolar bone. In conclusion, the strategy of loading EGCG in borosilicate glass shows great clinical promise in the treatment of alveolar defects in diabetic patients.

Ethics approval and consent to participate

To evaluate the effect and possible mechanism of EGCG on the repair of alveolar bone defects in diabetic rats. Sprague- Dawley (SD) male rats were selected for animal experiments and were purchased from Beijing Vitehe Laboratory Animal Technology Co. All experiments were performed at the Shenzhen Institute of Advanced Technology (SIAT) of the Chinese Academy of Sciences in accordance with the regulations of the SIAT Animal Research Committee.

Funding

Data and materials availability

All data needed to evaluate the conclusions in the paper are present in the paper and/or the Supplementary Materials. Additional data related to this paper may be requested from the authors.

CRediT authorship contribution statement

Pengfei Tian: Methodology, Validation, Data curation, Writing –

original draft. **Liming Zhao:** Methodology, Validation, Data curation, Writing – original draft. **Jua Kim:** Validation, Writing – review & editing. **Xian Li:** Methodology, Validation, Data curation. **Chunyu Liu:** Methodology, Visualization. **Xu Cui:** Validation. **Tao Liang:** Validation. **Yunbo Du:** Validation. **Xiehui Chen:** Validation. **Haobo Pan:** Funding acquisition, Investigation, Supervision, Resources, Writing – review & editing.

Declaration of competing interest

The authors declare that they have no known competing financial interests or personal relationships that could have appeared to influence the work reported in this paper.

Appendix A. Supplementary data

Supplementary data to this article can be found online at https://doi.org/10.1016/j.bioactmat.2023.02.023.

References

[1] E. Ahmad, S. Lim, R. Lamptey, D.R. Webb, M.J. Davies, Type 2 diabetes, Lancet (2022), https://doi.org/10.1016/S0140-6736(22)01655-5. S0140673622016555.

[2] H.-T. Cheng, X. Xu, P.S. Lim, K.-Y. Hung, Worldwide epidemiology of diabetes-related end-stage renal disease, 2000–2015, Diabetes Care 44 (2021) 89–97, https://doi.org/10.2337/dc20-1913.

[3] E.P. Joslin, Diabetes mellitus, N. Engl. J. Med. 236 (1947) 474–480, https://doi.org/10.1056/NEJM194703272361305.

[4] J.E. Kanter, K.E. Bornfeldt, Impact of diabetes mellitus, ATVB 36 (2016) 1049–1053, https://doi.org/10.1161/ATVBAHA.116.307302.

[5] B. Lecka-Czernik, Diabetes, bone and glucose-lowering agents: basic biology, Diabetologia 60 (2017) 1163–1169, https://doi.org/10.1007/s00125-017-4269-4.

[6] J. Liu, J. Ruan, M.D. Weir, K. Ren, A. Schneider, P. Wang, T.W. Oates, X. Chang, H. H.K. Xu, Periodontal bone-ligament-cementum regeneration via scaffolds and stem cells, Cells 8 (2019) 537, https://doi.org/10.3390/cells8060537.

[7] B. Tan, Q. Tang, Y. Zhong, Y. Wei, L. He, Y. Wu, J. Wu, J. Liao, Biomaterial-based strategies for maxillofacial tumour therapy and bone defect regeneration, Int. J. Oral Sci. 13 (2021) 9, https://doi.org/10.1038/s41368-021-00113-9.

[8] W. Wang, K.W.K. Yeung, Bone grafts and biomaterials substitutes for bone defect repair: a review, Bioact. Mater. 2 (2017) 224–247, https://doi.org/10.1016/j.bioactmat.2017.05.007.

[9] H. Jiao, E. Xiao, D.T. Graves, Diabetes and its effect on bone and fracture healing, Curr. Osteoporos. Rep. 13 (2015) 327–335, https://doi.org/10.1007/s11914-015-0286-8.

[10] J.M. Forbes, M.E. Cooper, Mechanisms of diabetic complications, Physiol. Rev. 93 (2013) 137–188, https://doi.org/10.1152/physrev.00045.2011.

[11] F. Giacco, M. Brownlee, Oxidative stress and diabetic complications, Circ. Res. 107 (2010) 1058–1070, https://doi.org/10.1161/CIRCRESAHA.110.223545.

[12] A.S. Baldwin, The NF-κB and IκB proteins: new discoveries and insights, Annu. Rev. Immunol. 14 (1996) 649–681, https://doi.org/10.1146/annurev.immunol.14.1.649.

[13] B. Hoesel, J.A. Schmid, The complexity of NF-κB signaling in inflammation and cancer, Mol. Cancer 12 (2013) 86, https://doi.org/10.1186/1476-4598-12-86.

[14] J. Zheng, S. Chen, M.L. Albiero, G.H.A. Vieira, J. Wang, J.Q. Feng, D.T. Graves, Diabetes activates periodontal ligament fibroblasts via NF-κB in vivo, J. Dent. Res. 97 (2018) 580–588, https://doi.org/10.1177/0022034518755697.

[15] K.I. Ko, A.L. Syverson, R.M. Kralik, J. Choi, B.P. DerGarabedian, C. Chen, D. T. Graves, Diabetes-induced NF-κB dysregulation in skeletal stem cells prevents resolution of inflammation, Diabetes 68 (2019) 2095–2106, https://doi.org/10.2337/db19-0496.

[16] M. Locati, G. Curtale, A. Mantovani, Diversity, mechanisms, and significance of macrophage plasticity, Annu. Rev. Pathol. 15 (2020) 123–147, https://doi.org/10.1146/annurev-pathmechdis-012418-012718.

[17] S.H. Kim, Y.K. Yeon, J.M. Lee, J.R. Chao, Y.J. Lee, Y.B. Seo, MdT. Sultan, O.J. Lee, J.S. Lee, S. Yoon, I.-S. Hong, G. Khang, S.J. Lee, J.J. Yoo, C.H. Park, Precisely printable and biocompatible silk fibroin bioink for digital light processing 3D printing, Nat. Commun. 9 (2018) 1620, https://doi.org/10.1038/s41467-018-03759-y.

[18] L. Pang, P. Tian, X. Cui, X. Wu, X. Zhao, H. Wang, D. Wang, H. Pan, In situ photo-cross-linking hydrogel accelerates diabetic wound healing through restored hypoxia-inducible factor 1-alpha pathway and regulated inflammation, ACS Appl. Mater. Interfaces 13 (2021) 29363–29379, https://doi.org/10.1021/acsami.1c07103.

[19] C. Chu, J. Deng, Y. Man, Y. Qu, Green tea extracts epigallocatechin-3-gallate for different treatments, BioMed Res. Int. (2017) 1–9, https://doi.org/10.1155/2017/5615647, 2017.

[20] C. Chu, L. Liu, Y. Wang, R. Yang, C. Hu, S. Rung, Y. Man, Y. Qu, Evaluation of epigallocatechin-3-gallate (EGCG)-modified scaffold determines macrophage recruitment, Mater. Sci. Eng. C 100 (2019) 505–513, https://doi.org/10.1016/j.msec.2019.03.007.

[21] C. Chu, Y. Wang, Y. Wang, R. Yang, L. Liu, S. Rung, L. Xiang, Y. Wu, S. Du, Y. Man, Y. Qu, Evaluation of epigallocatechin-3-gallate (EGCG) modified collagen in guided bone regeneration (GBR) surgery and modulation of macrophage phenotype, Mater. Sci. Eng. C 99 (2019) 73–82, https://doi.org/10.1016/j.msec.2019.01.083.

[22] O.M. Ighodaro, Molecular pathways associated with oxidative stress in diabetes mellitus, Biomed. Pharmacother. 108 (2018) 656–662, https://doi.org/10.1016/j.biopha.2018.09.058.

[23] C. Chu, J. Deng, L. Xiang, Y. Wu, X. Wei, Y. Qu, Y. Man, Evaluation of epigallocatechin-3-gallate (EGCG) cross-linked collagen membranes and concerns on osteoblasts, Mater. Sci. Eng. C 67 (2016) 386–394, https://doi.org/10.1016/j.msec.2016.05.021.

[24] C. Chu, J. Deng, Y. Man, Y. Qu, Evaluation of nanohydroxyapaptite (nano-HA) coated epigallocatechin-3-gallate (EGCG) cross-linked collagen membranes, Mater. Sci. Eng. C 78 (2017) 258–264, https://doi.org/10.1016/j.msec.2017.04.069.

[25] E.L. Mills, B. Kelly, A. Logan, A.S.H. Costa, M. Varma, C.E. Bryant, P. Tourlomousis, J.H.M. Däbritz, E. Gottlieb, I. Latorre, S.C. Corr, G. McManus, D. Ryan, H.T. Jacobs, M. Szibor, R.J. Xavier, T. Braun, C. Frezza, M.P. Murphy, L.A. O'Neill, Succinate dehydrogenase supports metabolic repurposing of mitochondria to drive inflammatory macrophages, Cell 167 (2016) 457–470.e13, https://doi.org/10.1016/j.cell.2016.08.064.

[26] P.H.G.M. Willems, R. Rossignol, C.E.J. Dieteren, M.P. Murphy, W.J.H. Koopman, Redox homeostasis and mitochondrial dynamics, Cell Metabol. 22 (2015) 207–218, https://doi.org/10.1016/j.cmet.2015.06.006.

[27] S. Willenborg, D.E. Sanin, A. Jais, X. Ding, T. Ulas, J. Nüchel, M. Popović, T. MacVicar, T. Langer, J.L. Schultze, A. Gerbaulet, A. Roers, E.J. Pearce, J. C. Brüning, A. Trifunovic, S.A. Eming, Mitochondrial metabolism coordinates stage-specific repair processes in macrophages during wound healing, Cell Metabol. 33 (2021) 2398–2414.e9, https://doi.org/10.1016/j.cmet.2021.10.004.

[28] Y. Yuan, Y. Chen, T. Peng, L. Li, W. Zhu, F. Liu, S. Liu, X. An, R. Luo, J. Cheng, J. Liu, Y. Lu, Mitochondrial ROS-induced lysosomal dysfunction impairs autophagic flux and contributes to M1 macrophage polarization in a diabetic condition, Clin. Sci. 133 (2019) 1759–1777, https://doi.org/10.1042/CS20190672.

[29] H. Khaliq, W. Jing, X. Ke, Y. Ke-Li, S. Peng-peng, L. Cui, Q. Wei-wei, L. Zhixin, L. Hua-Zhen, S. Hui, Z. Ju-Ming, P. Ke-Mei, Boron affects the development of the kidney through modulation of apoptosis, antioxidant capacity, and Nrf2 pathway in the african ostrich chicks, Biol. Trace Elem. Res. 186 (2018) 226–237, https://doi.org/10.1007/s12011-018-1280-7.

[30] I. Dikic, Z. Elazar, Mechanism and medical implications of mammalian autophagy, Nat. Rev. Mol. Cell Biol. 19 (2018) 349–364, https://doi.org/10.1038/s41580-018-0003-4.

[31] A. Kuma, M. Komatsu, N. Mizushima, Autophagy-monitoring and autophagy-deficient mice, Autophagy 13 (2017) 1619–1628, https://doi.org/10.1080/15548627.2017.1343770.

[32] V. Deretic, Autophagy in inflammation, infection, and immunometabolism, Immunity 54 (2021) 437–453, https://doi.org/10.1016/j.immuni.2021.01.018.

[33] X. Han, S. Sun, Y. Sun, Q. Song, J. Zhu, N. Song, M. Chen, T. Sun, M. Xia, J. Ding, M. Lu, H. Yao, G. Hu, Small molecule-driven NLRP3 inflammation inhibition via interplay between ubiquitination and autophagy: implications for Parkinson disease, Autophagy 15 (2019) 1860–1881, https://doi.org/10.1080/15548627.2019.1596481.

[34] M. Biasizzo, N. Kopitar-Jerala, Interplay between NLRP3 inflammasome and autophagy, Front. Immunol. 11 (2020), 591803, https://doi.org/10.3389/fimmu.2020.591803.

[35] Y. Wang, B. Liang, W.B. Lau, Y. Du, R. Guo, Z. Yan, L. Gan, W. Yan, J. Zhao, E. Gao, W. Koch, X.-L. Ma, Restoring diabetes-induced autophagic flux arrest in ischemic/reperfused heart by ADIPOR (adiponectin receptor) activation involves both AMPK-dependent and AMPK-independent signaling, Autophagy 13 (2017) 1855–1869, https://doi.org/10.1080/15548627.2017.1358848.

[36] N. Germic, Z. Frangez, S. Yousefi, H.-U. Simon, Regulation of the innate immune system by autophagy: monocytes, macrophages, dendritic cells and antigen presentation, Cell Death Differ. 26 (2019) 715–727, https://doi.org/10.1038/s41418-019-0297-6.

[37] J. Pajarinen, T. Lin, E. Gibon, Y. Kohno, M. Maruyama, K. Nathan, L. Lu, Z. Yao, S. B. Goodman, Mesenchymal stem cell-macrophage crosstalk and bone healing, Biomaterials 196 (2019) 80–89, https://doi.org/10.1016/j.biomaterials.2017.12.025.

[38] L.Y. Lu, F. Loi, K. Nathan, T. Lin, J. Pajarinen, E. Gibon, A. Nabeshima, L. Cordova, E. Jämsen, Z. Yao, S.B. Goodman, Pro-inflammatory M1 macrophages promote Osteogenesis by mesenchymal stem cells via the COX-2-prostaglandin E2 pathway: macrophages promote osteogenesis via COX-2, J. Orthop. Res. 35 (2017) 2378–2385, https://doi.org/10.1002/jor.23553.

[39] J.R. Dave, S.S. Chandekar, S. Behera, K.U. Desai, P.M. Salve, N.B. Sapkal, S. T. Mhaske, A.M. Dewle, P.S. Pokare, M. Page, A. Jog, P.A. Chivte, R.K. Srivastava, G.B. Tomar, Human gingival mesenchymal stem cells retain their growth and immunomodulatory characteristics independent of donor age, Sci. Adv. 8 (2022), https://doi.org/10.1126/sciadv.abm6504 eabm6504.

[40] L. Shang, J. Shao, S. Ge, Immunomodulatory functions of oral mesenchymal stem cells: novel force for tissue regeneration and disease therapy, J. Leukoc. Biol. 110 (2021) 539–552, https://doi.org/10.1002/JLB.3MR0321-766R.

[41] W. Jiang, J. Xu, Immune Modulation by Mesenchymal Stem Cells, (n.d) 16.

[42] K.-H. Tsai, W.-J. Wang, C.-W. Lin, P. Pai, T.-Y. Lai, C.-Y. Tsai, W.-W. Kuo, NADPH oxidase-derived superoxide Anion-induced apoptosis is mediated via the JNK-dependent activation of NF-κB in cardiomyocytes exposed to high glucose, J. Cell. Physiol. 227 (2012) 1347–1357, https://doi.org/10.1002/jcp.22847.

[43] M.J. Morgan, Z. Liu, Crosstalk of reactive oxygen species and NF-κB signaling, Cell Res. 21 (2011) 103–115, https://doi.org/10.1038/cr.2010.178.

[44] M. Morikawa, R. Derynck, K. Miyazono, TGF-B and the TGF-β family: context-dependent roles in cell and tissue physiology, Cold Spring Harbor Perspect. Biol. 8 (2016) a021873, https://doi.org/10.1101/cshperspect.a021873.

[45] T. Alliston, TGF-beta-induced repression of CBFA1 by Smad3 decreases cbfa1 and osteocalcin expression and inhibits osteoblast differentiation, EMBO J. 20 (2001) 2254–2272, https://doi.org/10.1093/emboj/20.9.2254.

[46] K. Janssens, P. ten Dijke, S. Janssens, W. Van Hul, Transforming growth factor-β1 to the bone, Endocr. Rev. 26 (2005) 743–774, https://doi.org/10.1210/er.2004-0001.

[47] S.A. Abdelnour, M.E. Abd El-Hack, A.A. Swelum, A. Perillo, C. Losacco, The vital roles of boron in animal health and production: a comprehensive review, J. Trace Elem. Med. Biol. 50 (2018) 296–304, https://doi.org/10.1016/j.jtemb.2018.07.018.